

# Assessment of turbulence models using DNS data of compressible plane free shear layer flow

D. Li<sup>1</sup>, J. Komperda<sup>1</sup>, A. Peyvan<sup>1</sup>, Z. Ghiasi<sup>1</sup> and F. Mashayek<sup>1,†</sup>

<sup>1</sup>Department of Mechanical and Industrial Engineering, University of Illinois at Chicago, Chicago, IL 60607, USA

(Received 28 February 2021; revised 15 August 2021; accepted 19 October 2021)

The present paper uses the detailed flow data produced by direct numerical simulation (DNS) of a three-dimensional, spatially developing plane free shear layer to assess several commonly used turbulence models in compressible flows. The free shear layer is generated by two parallel streams separated by a splitter plate, with a naturally developing inflow condition. The DNS is conducted using a high-order discontinuous spectral element method (DSEM) for various convective Mach numbers. The DNS results are employed to provide insights into turbulence modelling. The analyses show that with the knowledge of the Reynolds velocity fluctuations and averages, the considered strong Reynolds analogy models can accurately predict temperature fluctuations and Favre velocity averages, while the extended strong Reynolds analogy models can correctly estimate the Favre velocity fluctuations and the Favre shear stress. The pressure–dilatation correlation and dilatational dissipation models overestimate the corresponding DNS results, especially with high compressibility. The pressure–strain correlation models perform excellently for most pressure–strain correlation components, while the compressibility modification model gives poor predictions. The results of an *a priori* test for subgrid-scale (SGS) models are also reported. The scale similarity and gradient models, which are non-eddy viscosity models, can accurately reproduce SGS stresses in terms of structure and magnitude. The dynamic Smagorinsky model, an eddy viscosity model but based on the scale similarity concept, shows acceptable correlation coefficients between the DNS and modelled SGS stresses. Finally, the Smagorinsky model, a purely dissipative model, yields low correlation coefficients and unacceptable accumulated errors.

**Key words:** free shear layers, compressible turbulence, shear layer turbulence

† Email address for correspondence: [mashayek@uic.edu](mailto:mashayek@uic.edu)

## 1. Introduction

Turbulence, the chaotic state of fluid flow in terms of pressure and velocity, is one of the most challenging fluid physics problems. A fundamental understanding of turbulence physics is essential for designing engineering systems because turbulence exists in nearly all macro engineering and atmospheric flows (Pope 2000). Traditionally, researchers have broadly classified the means to study turbulent flows into analytical theory, physical experiment and numerical simulation (Scheffel 2001).

Navier–Stokes equations are widely used to model turbulent flows such as hurricanes, ocean currents and flows behind high-speed vehicles. However, analytical solutions to Navier–Stokes equations have only been attainable with many assumptions, such as one-dimensional (1-D) geometry, constant specific heats, constant viscosity or equation linearization. However, experiments are often costly and face challenges to collect comprehensive information of the laminar–turbulent transition process and many turbulent quantities, such as the spanwise normal stress, turbulent kinetic energy dissipation and higher-order correlations. Certain unmeasurable flow properties in the flow field can be approximated by strong Reynolds analogy (SRA) (Morkovin 1962; Cebeci & Smith 1974) or extended strong Reynolds analogy (ESRA) models (Bradshaw 1977; Gaviglio 1987; Barre, Quine & Dussauge 1994; Lele 1994; Huang, Coleman & Bradshaw 1995; Duan & Martin 2011; Zhang *et al.* 2014; Barre & Bonnet 2015), but with strict conditions such as insignificant temperature and density fluctuations. In contrast, the numerical simulation of turbulence has become popular owing to the exponential computing power growth in the last several decades. Numerical simulations have empowered researchers and designers to explore deeper and broader into the details of the system behaviour than what experiment can. Based on the degree of the representation of the accuracy and physics, we can classify the numerical simulation methodologies into direct numerical simulation (DNS), large-eddy simulation (LES) and Reynolds-averaged Navier–Stokes (RANS) simulation.

Each numerical simulation approach possesses its own advantages and disadvantages. So far, DNS is only able to simulate simple flow configurations with low Reynolds numbers owing to the limitation in computational resources. The RANS approach is intrinsically less accurate and unable to provide detailed information about the flow field although it is computationally efficient. It is still widely used in engineering practice because the averaged flow field's reasonable prediction is adequate for design. Since the late 1950s, RANS modelling has progressed to second-order closure turbulence models. The performance of the second-order closure models manifests a significant improvement over that of simple turbulence models. Studies of some typical RANS models can be found in the literature (Launder, Reece & Rodi 1975; Hanjalic & Launder 1976; Launder 1989; Sarkar *et al.* 1989, 1991; Speziale, Sarkar & Gatski 1991; Ristorcelli, Lumley & Abid 1995; Hwang & Jaw 1998; Jaw & Chen 1998*a*, ; Girimaji 2000; Yoder 2003; Carlson 2005; Gross, Blaisdell & Lyrintzis 2011; Dudek & Carlson 2017). The LES approach situates in between DNS and RANS in computational cost. Large-eddy simulation is more accurate and reliable than RANS simulation for turbulent flows in which large-scale unsteadiness is significant, because LES can resolve large-scale structures without modelling (Pope 2000). Additionally, LES can provide more insights into fundamental physics owing to the available instantaneous flow structures. Large-eddy simulation has become a desirable approach to study flows dominated by large-scale coherent structures (Pope 2000), such as the plane free shear layer.

Recently, owing to the rapid advances in computational power, improved subgrid-scale (SGS) models have been continuously proposed since the first practical SGS model

developed by Smagorinsky (1963). However, none of them has accomplished the combination of accuracy and efficiency to make LES the preferred turbulence modelling approach for engineers and scientists (Burton & Dahm 2005). Therefore, the development of accurate and efficient SGS models has been a major task. The SGS stresses appear as essential terms for modelling in LES (Vreman, Geurts & Kuerten 1997). Thus, intense efforts have been put into developing sophisticated SGS models, which are able to simulate wall-bounded or non-wall-bounded turbulent flows, e.g. the wall-adapting local eddy-viscosity (WALE) and Sigma models (Nicoud & Ducros 1999; Nicoud *et al.* 2011). Many researchers attempted to validate the SGS models using DNS data at relatively low Reynolds numbers (Clark, Ferziger & Reynolds 1979; Love 1980; Piomelli *et al.* 1990; Zang, Dahlburg & Dahlburg 1992; Vreman, Geurts & Kuerten 1995a; Vreman *et al.* 1997; Okong'o & Bellan 2004; Selle *et al.* 2007; Nicoud *et al.* 2011). In such SGS model validations, *a priori* and *a posteriori* tests (Piomelli *et al.* 1990) are often used. The *a priori* test is performed by filtering the DNS data to compute the turbulent SGS stresses and comparing these quantities with stresses provided by SGS models (Vreman *et al.* 1995a). However, the *a posteriori* test involves real LES simulations, and the results are used to compare with DNS data (Vreman *et al.* 1995a). In the present paper, we adopt the *a priori* test for the SGS model examination.

The evaluation of turbulence models in a spatially developing turbulent free shear layer with naturally developing inflow condition is not currently available in the literature. The performance of some typical turbulence models in the laminar, transition and turbulent regions of such a flow is still unclear. Additionally, the sensitivity of turbulence models to the change of Mach number is not fully understood. In this context, we perform a comparative study of some typical turbulence models using DNS data generated by a high-order discontinuous spectral element method (DSEM) code (Kopriva & Koliaas 1996; Kopriva 1998; Jacobs, Kopriva & Mashayek 2005). This DSEM code has been employed for LES and DNS of compressible turbulent flows (Ghiasi *et al.* 2019; Li *et al.* 2019, 2021) as well as reacting flows (Komperda *et al.* 2020). We do not concentrate on numerical methods but systematically examine and compare the characteristic behaviour of several SRA, RANS and LES models for a three-dimensional (3-D), compressible plane free shear layer. This primary objectives of this work are: (1) to identify and explain the performance of the SRA, RANS and SGS models; (2) to provide a basis for future modelling of a spatially developing, compressible free shear flow in the laminar, transition and turbulent regions. The remainder of this paper is organized as follows. First, we provide a brief overview of the DNS data. Then, the comparisons and discussions of different turbulent models are presented. Finally, we provide a summary of the findings.

## 2. Direct numerical simulation

In this section, we briefly describe the DNS of the 3-D, compressible turbulent plane free shear layer flow that has been reported in detail in our previous papers (Li *et al.* 2019, 2021).

### 2.1. Compressible Navier–Stokes equations

The compressible Navier–Stokes equations govern the viscous fluid flow and are solved in conservative form. Variables are non-dimensionalized by the reference length,  $L_f^*$ , density,  $\rho_f^*$ , velocity,  $U_f^*$ , and temperature,  $T_f^*$ . The superscript \* denotes dimensional quantities and the subscript  $f$  indicates reference values. The non-dimensionalized variables are

defined as

$$\left. \begin{aligned} x_j &= x_j^*/L_f^*, & \rho &= \rho^*/\rho_f^*, \\ u_i &= u_i^*/U_f^*, & t &= t^*/(L_f^*/U_f^*), \\ T &= T^*/T_f^*, & p &= p^*/(\rho_f^*U_f^{*2}), \\ \gamma &= c_p^*/c_v^*, & Pr &= c_p^*\mu^*/\kappa^*, \\ M_f &= U_f^*/\sqrt{\gamma R^*T_f^*}, & Re_f &= U_f^*L_f^*\rho_f^*/\mu^*, \end{aligned} \right\} \quad (2.1)$$

where  $x_j$  is the  $j$ th Cartesian coordinate. Also,  $p$ ,  $\gamma$  and  $\mu$  are pressure, specific heats ratio and dynamic viscosity, respectively. Moreover,  $c_v$ ,  $c_p$ ,  $\kappa$  and  $R$  represent the specific heat at constant volume, specific heat at constant pressure, thermal conductivity and gas constant, respectively. The Prandtl number, reference Mach number and reference Reynolds number are respectively indicated by  $Pr$ ,  $M_f$  and  $Re_f$ . These lead to the following non-dimensional Navier–Stokes equations, presented in a conservative form in Cartesian tensor notation,

$$\frac{\partial \rho}{\partial t} + \frac{\partial(\rho u_j)}{\partial x_j} = 0, \quad (2.2)$$

$$\frac{\partial(\rho u_i)}{\partial t} + \frac{\partial(\rho u_i u_j)}{\partial x_j} = -\frac{\partial p}{\partial x_i} + \frac{\partial \sigma_{ij}}{\partial x_j}, \quad (2.3)$$

$$\frac{\partial(\rho e)}{\partial t} + \frac{\partial[(\rho e + p)u_j]}{\partial x_j} = -\frac{\partial q_j}{\partial x_j} + \frac{\partial(\sigma_{ij}u_i)}{\partial x_j}. \quad (2.4)$$

Here, the total energy term, viscous stress tensor and heat flux vector are respectively defined as

$$\rho e = \frac{p}{\gamma - 1} + \frac{1}{2}\rho u_k u_k, \quad (2.5)$$

$$\sigma_{ij} = \frac{1}{Re_f} \left( \frac{\partial u_i}{\partial x_j} + \frac{\partial u_j}{\partial x_i} - \frac{2}{3} \frac{\partial u_k}{\partial x_k} \delta_{ij} \right), \quad (2.6)$$

$$q_j = -\frac{1}{(\gamma - 1)Re_f Pr M_f^2} \frac{\partial T}{\partial x_j}, \quad (2.7)$$

where  $\delta_{ij}$  is the Kronecker delta. In this study, the specific heat, thermal conductivity and dynamic viscosity of the fluid are assumed to be constant because the temperature fluctuations in all considered simulations are insignificant ( $< 6\%$ ) (Li *et al.* 2021). The equation of state closes the equations mentioned above, and is given as

$$p = \frac{\rho T}{\gamma M_f^2}. \quad (2.8)$$

The total energy can be also expressed as

$$\rho e = \frac{\rho T}{(\gamma - 1)\gamma M_f^2} + \frac{1}{2}\rho u_k u_k, \quad (2.9)$$

which is convenient when applying Reynolds averaging or Favre averaging to the energy conservation equation.

2.2. Discontinuous spectral element method

This work employs the DSEM as the compressible turbulent flow solver (Jacobs *et al.* 2005). The physical geometry is partitioned into 3-D hexahedral elements. The DSEM then uses the isoparametric mapping to map each element onto a unit cube in every direction. After mapping, (2.2)–(2.4) read

$$\frac{\partial \widehat{\rho}}{\partial t} + \frac{\partial(\widehat{\rho u_j})}{\partial X_j} = 0, \tag{2.10}$$

$$\frac{\partial(\widehat{\rho u_i})}{\partial t} + \frac{\partial(\widehat{\rho u_i u_j} + p \delta_{ij})}{\partial X_j} = \frac{\partial \widehat{\sigma_{ij}}}{\partial X_j}, \tag{2.11}$$

$$\frac{\partial(\widehat{\rho e})}{\partial t} + \frac{\partial[(\widehat{\rho e} + p)u_j]}{\partial X_j} = -\frac{\partial \widehat{q_j}}{\partial X_j} + \frac{\partial(\widehat{\sigma_{ij} u_i})}{\partial X_j}. \tag{2.12}$$

For (2.10),

$$\widehat{\rho} = J\rho; \quad (\widehat{\rho u_j}) = J \frac{\partial X_j}{\partial x_i}(\rho u_i); \tag{2.13a,b}$$

for (2.11),

$$(\widehat{\rho u_i}) = J(\rho u_i); \quad (\widehat{\rho u_i u_j} + p \delta_{ij}) = J \frac{\partial X_j}{\partial x_i}(\rho u_j u_i + p \delta_{ji}); \quad \widehat{\sigma_{ij}} = J \frac{\partial X_j}{\partial x_i} \sigma_{ji}; \tag{2.14a-c}$$

and for (2.12),

$$\begin{aligned} (\widehat{\rho e}) &= J(\rho e); \quad [(\widehat{\rho e} + p)u_j] = J \frac{\partial X_j}{\partial x_i}[(\rho e + p)u_i]; \\ \widehat{q_j} &= J \frac{\partial X_j}{\partial x_i} q_i; \quad (\widehat{\sigma_{ij} u_i}) = J \frac{\partial X_j}{\partial x_i}(\sigma_{ji} u_j). \end{aligned} \tag{2.15a-d}$$

In the above equations,  $J$  is defined as (Jacobs 2003)

$$\begin{aligned} J(X_1, X_2, X_3) &= \frac{\partial x_1}{\partial X_1} \left( \frac{\partial x_2}{\partial X_2} \frac{\partial x_3}{\partial X_3} - \frac{\partial x_2}{\partial X_3} \frac{\partial x_3}{\partial X_2} \right) - \frac{\partial x_1}{\partial X_2} \left( \frac{\partial x_2}{\partial X_1} \frac{\partial x_3}{\partial X_3} - \frac{\partial x_2}{\partial X_3} \frac{\partial x_3}{\partial X_1} \right) \\ &+ \frac{\partial x_1}{\partial X_3} \left( \frac{\partial x_2}{\partial X_1} \frac{\partial x_3}{\partial X_2} - \frac{\partial x_2}{\partial X_2} \frac{\partial x_3}{\partial X_1} \right), \end{aligned} \tag{2.16}$$

which is the determinant of the Jacobian matrix of the transformation. The term  $\partial X_i / \partial x_j$  denotes the metrics matrix, where  $x_j$  and  $X_i$  are the coordinates of the physical and mapped spaces, respectively. The variables with hat  $\widehat{\phantom{x}}$  are in the mapped space, whereas those without a hat are in the physical space.

In each mapped element, high-order Lagrange basis functions estimate the primitive variables and the fluxes on the Gauss quadrature and Lobatto quadrature points, respectively. Gauss quadrature and Lobatto quadrature points are respectively defined as

$$X_{j+1/2} = \frac{1}{2} \left\{ 1 - \cos \left[ \frac{(2j+1)\pi}{2N} \right] \right\}, \quad j = 0, \dots, N-1, \tag{2.17}$$

and

$$X_j = \frac{1}{2} \left\{ 1 - \cos \left[ \frac{\pi j}{N} \right] \right\}, \quad j = 0, \dots, N, \tag{2.18}$$

within the unit cube. Here,  $N-1$  is the polynomial order of the spectral element. For convenience, we refer to  $N-1$  as  $\zeta$  hereafter. Finally, the primitive variable,  $\widehat{\rho}$ , on the

$M_c$	VR	$\Delta U$	$M_1$	$M_2$	$x_R$	$x_E$
0.3	0.54	2.1	0.8556	0.2556	30	340
0.5	0.54	3.5	1.4259	0.4259	170	550
0.7	0.54	4.9	1.9963	0.5963	230	670

Table 1. Some simulation parameters and estimated flow properties. Here,  $M_c = \Delta U / (c_1 + c_2)$  (Bogdanoff 1983), where  $c_1$  and  $c_2$  are respectively the speeds of sound in the high- and low-speed streams of the shear layer. The inflow Mach numbers on the high- and low-speed sides are respectively indicated by  $M_1 = U_1 / c_1$  and  $M_2 = U_2 / c_2$ . Finally,  $x_R$  represents the location where the transition starts, while  $x_E$  denotes the location where the transition to turbulent flow ends (see Li *et al.* (2019) for more detail).

Gauss quadrature points, for example, is estimated as

$$\hat{\rho}(X, Y, Z) = \sum_{i=0}^{\xi} \sum_{j=0}^{\xi} \sum_{k=0}^{\xi} \hat{\rho}_{i+1/2, j+1/2, k+1/2} h_{i+1/2}(X) h_{j+1/2}(Y) h_{k+1/2}(Z). \quad (2.19)$$

Here,  $X$ ,  $Y$  and  $Z$  indicate the mapped space coordinates, while  $h_{j+1/2}$  denotes the Lagrange interpolating polynomial on the Gauss points. A fourth-order low-storage Runge–Kutta scheme (Carpenter & Kennedy 1994) is adopted for time integration after the viscous and inviscid fluxes are calculated.

### 2.3. Simulation parameters

The computational domain, as shown in figure 1, is enclosed with inflow and outflow boundaries (Jacobs, Kopriva & Mashayek 2003) in the streamwise direction, non-reflecting boundaries (Thompson 1987) in the cross-stream direction and periodic boundaries (Jacobs *et al.* 2003) in the spanwise direction. The high- and low-speed streams at the inlet are set to fulfil a velocity ratio,  $VR = 0.54$ , which is given as

$$VR = \frac{U_1 - U_2}{U_1 + U_2} = \frac{\Delta U}{U_1 + U_2}. \quad (2.20)$$

Three simulations are conducted for various inflow Mach numbers and convective Mach numbers, as given in table 1. The momentum thickness Reynolds number,  $Re_\theta$ , based on  $\Delta U$  and  $\delta_{\theta 0}$ , is 140, where  $\delta_{\theta 0}$  is the initial momentum thickness. The momentum thickness is defined as (Jiménez 2004)

$$\delta_\theta = \frac{1}{\rho_o} \int_{-\infty}^{+\infty} \langle \rho \rangle \frac{\{u\} - U_2}{\Delta U} \left( 1 - \frac{\{u\} - U_2}{\Delta U} \right) dy, \quad (2.21)$$

for a spatially evolving compressible plane free shear layer. Here,  $\rho_o$  indicates the initial inflow density, and  $\langle \rho \rangle$  and  $\{u\}$  are respectively the Reynolds-averaged density and Favre-averaged velocity (Favre 1969). A pair of angled brackets,  $\langle \rangle$ , denotes a Reynolds average, and a pair of curly brackets,  $\{ \}$ , indicates a Favre average. To compute Reynolds and Favre averages, we start with Reynolds decomposition (Favre 1969), which is defined as

$$\phi = \langle \phi \rangle + \phi', \quad (2.22)$$

for any variable  $\phi$ . Here,  $\phi'$  is the turbulent fluctuation from the Reynolds average indicated by the superscript  $'$ . The Reynolds average,  $\langle \phi \rangle$ , can be obtained from an average in time,

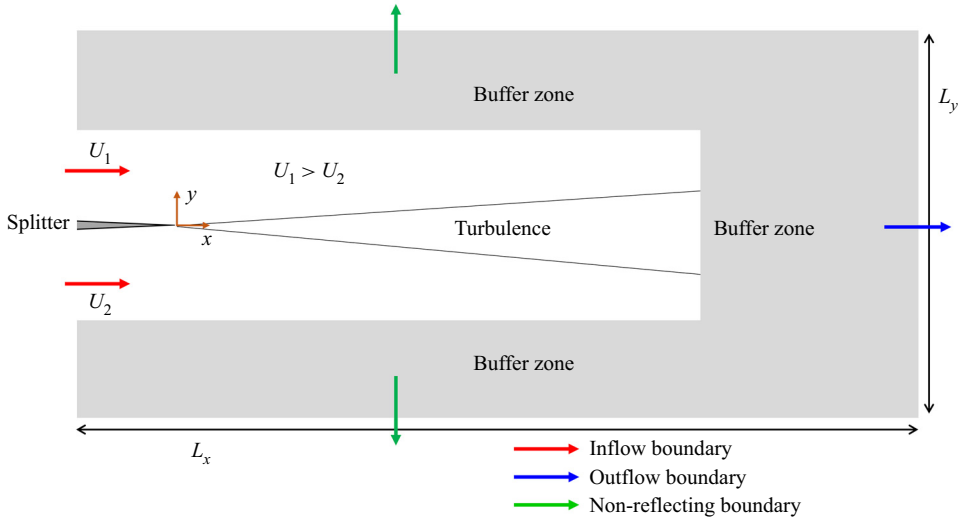


Figure 1. Schematic of the computational domain.

space or an ensemble average. Similarly, Favre decomposition is defined as (Favre 1969)

$$\phi = \{\phi\} + \phi'', \tag{2.23}$$

where  $\phi''$  is the turbulent fluctuation with respect to the Favre average denoted by the superscript  $''$ . The Favre average,  $\{\phi\}$ , is defined as

$$\{\phi\} = \langle \rho \phi \rangle / \langle \rho \rangle. \tag{2.24}$$

Note that

$$\langle \phi' \rangle = 0; \quad \langle \rho \phi'' \rangle = 0; \quad \langle \phi'' \rangle \neq 0. \tag{2.25a-c}$$

Finally, the specific heats ratio,  $\gamma$ , and the reference Prandtl number,  $Pr_f$ , are respectively taken as 1.4 and 0.7.

#### 2.4. Initial conditions

In this work, the shear layer is formed by two parallel laminar boundary layers, with naturally developing inflow condition and separated by a splitter plate. The two fully developed Blasius boundary layers traverse the trailing edge of the splitter plate and merge into a free shear layer downstream. The configuration of the splitter plate is illustrated in figure 1. A small perturbation is superimposed on the high-speed side boundary layer (Li *et al.* 2019). The low-speed stream is laminar without perturbations. The dimensionless density and temperature are uniformly initialized to 1.0 and  $(\Delta U / 2M_c)^2$ , respectively. Note that the trace of the initial conditions has been fully purged as the flow attains self-similarity (Bradshaw 1966) (see Li *et al.* (2019) for the detailed description of the free shear layer initial conditions).

#### 2.5. Computational domain and grid

All dimensions are normalized by  $\delta_{\theta 0}$ . The size of the domain is set as  $L_x \times L_y \times L_z = 1982 \times 1600 \times 140$ , as shown in figure 1. The area of interest is  $0 \leq x \leq 1200$  used

for producing DNS data. The remainder is used as a vast buffer zone to avoid solution contamination from cross-stream and outlet boundaries (see [figure 1](#)). The computational grid contains 1 368 260 elements and 295 544 160 solution points for a polynomial order of five. With the relatively low Reynolds number ( $Re = 140$ ) considered in this work, the resolution of the current grid is sufficient to capture all relevant turbulent scales. A detailed validation against published theoretical, experimental and numerical results has been performed and excellent agreements have been found (Li *et al.* 2019). To acquire the necessary statistics, every simulation is first run for five flow-through times to eliminate the transient flow and accomplish a quasi-stationary state. The flow-through time is the time required for the flow to move with the convective velocity from the inlet to the outlet, i.e.

$$\text{flow-through time} = \frac{L_x}{U_c}, \tag{2.26}$$

where the convective velocity  $U_c$  is defined as

$$U_c = \frac{U_1 + U_2}{2}, \tag{2.27}$$

when the specific heats ratio is assumed to be constant across the shear layer. Second, five flow-through times are required to calculate the first-order statistics. Third, ten flow-through times are needed to acquire sufficient data for the second-order statistics. Finally, we implement post-processing for ensemble averages in the spanwise direction to enhance the accuracy of the statistics. The details of the problem set-up and solution validation are reported in previous work (Li *et al.* 2019, 2021).

### 3. Strong Reynolds analogy

When developing turbulence models for compressible flows, researchers often start with Morkovin’s hypothesis – strong Reynolds analogy (Morkovin 1962). Morkovin suggested that the effect of high speed is reflected by the change of fluid properties. However, the high-speed effect does not directly affect the dynamic behaviour of turbulence for moderate Mach numbers (Morkovin 1962). Thus, to properly apply Morkovin’s hypothesis, the temperature fluctuations are often required to be negligible, which is valid for the present study. In this section, we examine this hypothesis. In other words, we attempt to show that it is possible to describe turbulent free shear flows using relatively straightforward SRA models.

In the turbulent free shear flow experiment, the measurements might give most of the flow properties in the flow field. However, no direct measurement of temperature fluctuation, or density fluctuation, or the correlation between temperature and velocity or the correlation between density and velocity has been realized. Using the SRA, the temperature and density fluctuations can be obtained from the measured velocity fluctuations. The fluctuations in temperature, density and velocity are related by (Morkovin 1962; Gaviglio 1987; Barre *et al.* 1994)

$$\frac{\sqrt{\langle T'^2 \rangle}}{\langle T \rangle} \approx \frac{\sqrt{\langle \rho'^2 \rangle}}{\langle \rho \rangle}, \tag{3.1}$$

and

$$\frac{\sqrt{\langle T'^2 \rangle}}{\langle T \rangle} = (\gamma - 1)M^2 \frac{\sqrt{\langle u'^2 \rangle}}{\langle u \rangle}, \tag{3.2}$$



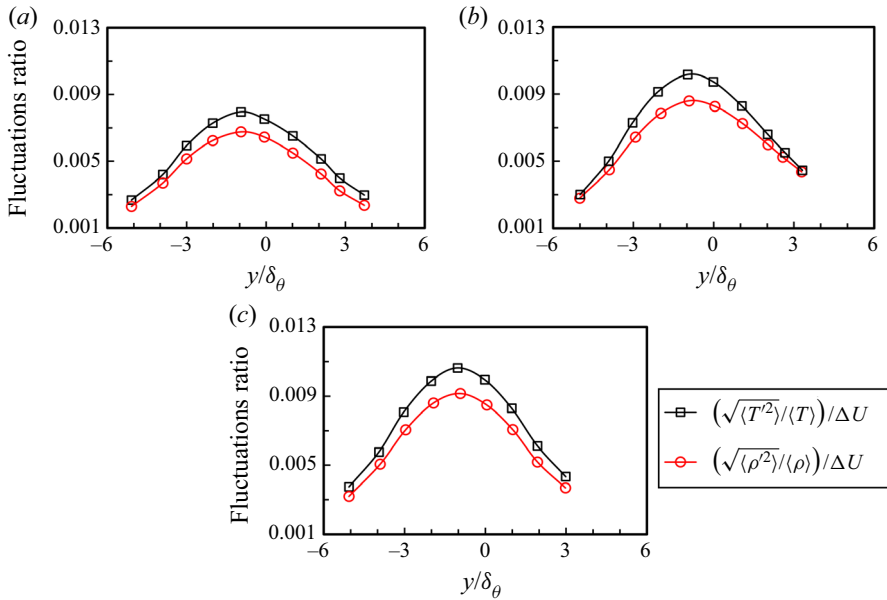


Figure 2. Cross-stream profiles of the values of the left-hand side (black squares) and right-hand side (red circles) of (3.1) with (a)  $M_c = 0.3$ , (b)  $M_c = 0.5$  and (c)  $M_c = 0.7$  at  $x - x_E = 300$ . All terms are normalized by  $(\Delta U)$ .

where  $M = \{u\}/c$  is the local Mach number. Figure 2 shows the variations of the normalized temperature fluctuation,  $(\sqrt{\langle T^2 \rangle} / \langle T \rangle) / (\Delta U)$ , and the normalized density fluctuation,  $(\sqrt{\langle \rho^2 \rangle} / \langle \rho \rangle) / (\Delta U)$ , across the shear layer. As can be seen, the maximum  $(\sqrt{\langle T^2 \rangle} / \langle T \rangle) / (\Delta U)$  is approximately 0.008 for  $M_c = 0.3$ , and increases to 0.011 as  $M_c$  increases to 0.7. However, for all cases,  $\sqrt{\langle T^2 \rangle} \ll \langle T \rangle$ , which is the condition that satisfies the requirement for applying SRA. Moreover, figure 2 indicates that the variation of the normalized density fluctuation approximately agrees with that of the temperature fluctuation in each case, which confirms the analogy relation defined by (3.1). Moreover, figure 3(a) shows a remarkable agreement between the temperature and velocity fluctuations, which confirms the analogy relation presented by (3.2). However, with increasing convective Mach number,  $[(\gamma - 1)M^2 \sqrt{\langle u^2 \rangle} / \langle u \rangle] / (\Delta U)$  increasingly overpredicts  $(\sqrt{\langle T^2 \rangle} / \langle T \rangle) / (\Delta U)$ , as shown in figures 3(b) and 3(c). This trend may arise from the fact that increasing the convective Mach number increases the temperature fluctuation. Consequently, the condition of applying the SRA model deviates away from the ideal assumption.

Under the condition of negligible temperature fluctuations, the Favre average can be expressed as a function of the Reynolds average and fluctuation (Gaviglio 1987; Barre et al. 1994; Barre & Bonnet 2015)

$$\{u\} \approx \langle u \rangle + \frac{(\gamma - 1)M^2}{\langle u \rangle} \langle u'^2 \rangle, \tag{3.3}$$

and

$$\{v\} \approx \langle v \rangle + \frac{(\gamma - 1)M^2}{\langle u \rangle} \langle u'v' \rangle. \tag{3.4}$$

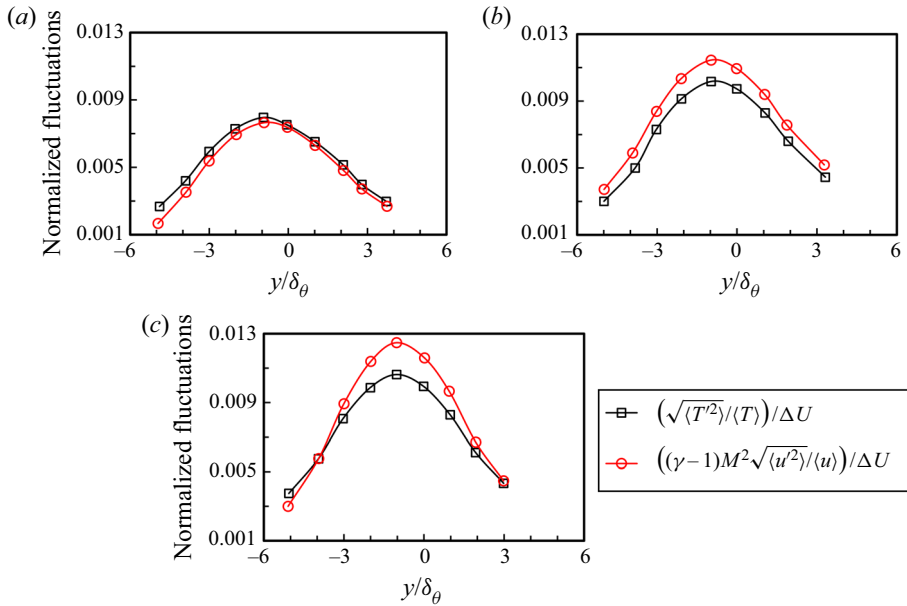


Figure 3. Cross-stream profiles of the values of the left-hand side (black squares) and right-hand side (red circles) of (3.2) with (a)  $M_c = 0.3$ , (b)  $M_c = 0.5$  and (c)  $M_c = 0.7$  at  $x - x_E = 300$ . All terms are normalized by  $(\Delta U)$ .

Equations (3.3) and (3.4) represent another form of SRA, which present the relations between the Favre and Reynolds quantities. The compressibility effect is reflected by the square of the Mach number in the equation. Figures 4 and 5 respectively compare the variations of left-hand side (black squares) and right-hand side (red circles) of (3.3) and (3.4). As can be seen, the left-hand side and right-hand side of the equations are in good agreement for various convective Mach numbers. This implies that the SRA performs excellently for different velocity components and convective Mach numbers.

Although the SRA predicts the relations among the fluctuations of the temperature, density and velocities well, it is insufficient to estimate the budget terms in the turbulent kinetic energy transport equation. Relations must be created for the triple correlations, such as  $\langle \rho u'' v'' \rangle$ . Those relations are called extended strong Reynolds analogy (ESRA) and can be expressed as (Barre *et al.* 1994; Barre & Bonnet 2015)

$$u'' \approx u' - \frac{(\gamma - 1)M^2}{\langle u \rangle} \langle u'^2 \rangle, \tag{3.5}$$

$$v'' \approx v' - \frac{(\gamma - 1)M^2}{\langle u \rangle} \langle u' v' \rangle, \tag{3.6}$$

$$\frac{\langle \rho u'' v'' \rangle}{\langle \rho \rangle} \approx \langle \rho u' v' \rangle + \frac{(\gamma - 1)M^2}{\langle u \rangle} \langle u'^2 v' \rangle - \frac{(\gamma - 1)^2 M^4}{\langle u \rangle^2} \langle u'^2 \rangle \langle u' v' \rangle. \tag{3.7}$$

Equations (3.5) and (3.6) express the relations between Favre and Reynolds fluctuations for streamwise and cross-stream velocities. Similarly, (3.7) presents the relation between the density-weighted shear stress term (the shear component in the  $x - y$  plane) and its expression in terms of Reynolds fluctuations. Figure 6 shows the cross-stream profiles of the left-hand side (black squares) and right-hand side (red circles) of (3.7) for  $M_c = 0.3$ ,

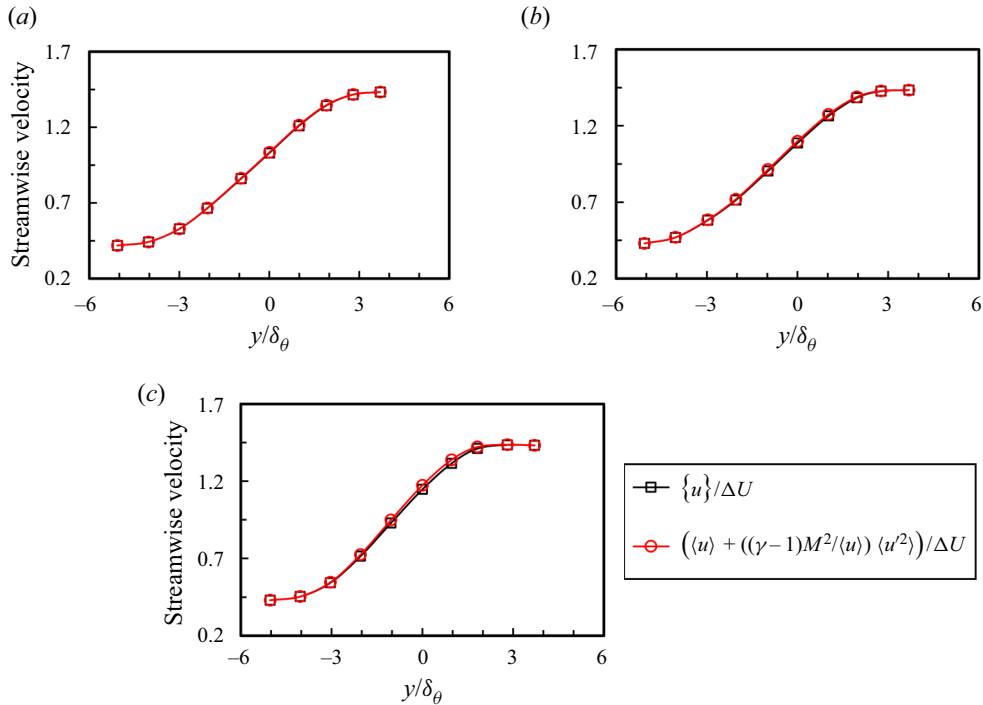


Figure 4. Cross-stream profiles of the values of the left-hand side (black squares) and right-hand side (red circles) of (3.3) with (a)  $M_c = 0.3$ , (b)  $M_c = 0.5$ , and (c)  $M_c = 0.7$ , at  $x - x_E = 300$ . All terms are normalized by  $(\Delta U)$ .

0.5 and 0.7. The data are extracted at  $x - x_E = 300$  and normalized by  $(\Delta U)^2$ . It can be seen that the left-hand side and right-hand side are in excellent agreement, which means that the ESRA model correctly estimates the most important component of the production term of the turbulent kinetic energy transport equation.

Figures 7 and 8 show the scatter plots of the temporal evolution data of the modelled and DNS Favre velocity fluctuations at a specific location for six flow-through times. Figure 7 compares DNS (left-hand side of (3.5)) with modelled (right-hand side of (3.5)) Favre streamwise velocity fluctuations for  $M_c = 0.3$  and 0.7. All terms are extracted at the centre of the shear layer (see table 2) and normalized by  $(\Delta U)$ . It can be seen that the left-hand side and right-hand side of (3.5) exhibit a high degree of correlation at both  $M_c = 0.3$  and 0.7. Strong correlation is also found in figure 8 representing (3.6) at the centre of the shear layer. Other locations, such as the upper and lower edges (see table 2) of the shear layer also showed similar behaviours for (3.5) and (3.6). For brevity, the comparisons at these locations are not included here.

To further compare the discrepancy between the left-hand side and right-hand side of (3.5) and (3.6), we compute the mean absolute deviation (MAD), which is defined as

$$MAD = \frac{1}{n} \sum_{i=1}^n |LHS_i - RHS_i|, \tag{3.8}$$

where  $n$  represents the number of samples. The computed MADs are tabulated in tables 3 and 4. Based on the data in tables 3 and 4, we can conclude the following: the largest correlation discrepancy is located at the centre of the shear layer for both (3.5) and

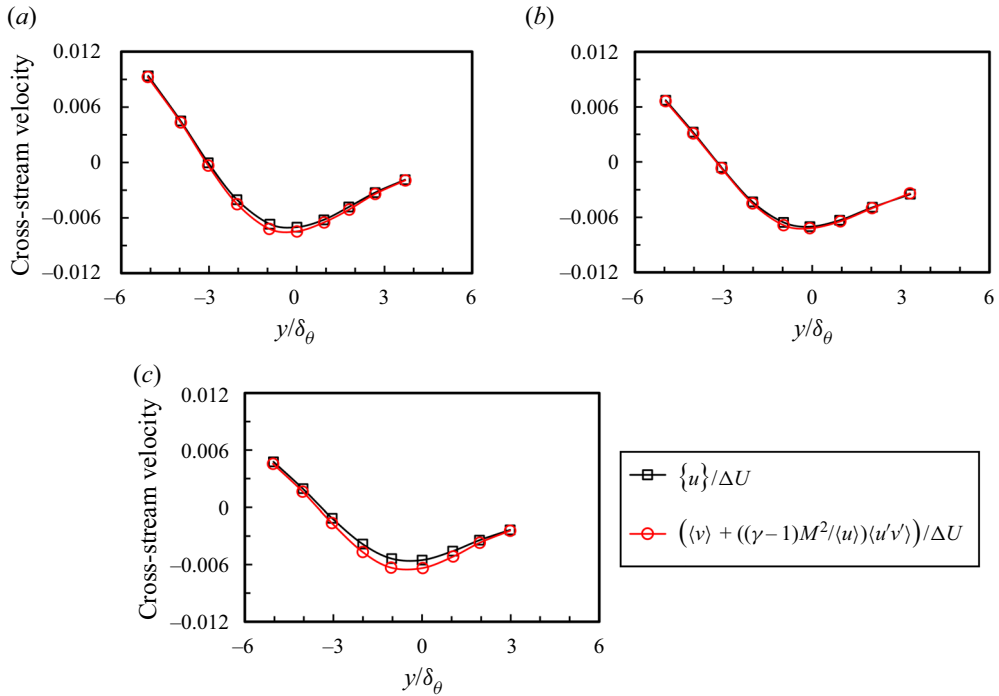


Figure 5. Cross-stream profiles of the values of the left-hand side (black squares) and right-hand side (red circles) of (3.4) with (a)  $M_c = 0.3$ , (b)  $M_c = 0.5$ , and (c)  $M_c = 0.7$ , at  $x - x_E = 300$ . All terms are normalized by  $(\Delta U)$ .

(3.6); the correlation discrepancy in (3.5) is larger than that in (3.6); the error in the high-Mach-number case is higher than that in the low-Mach-number case.

#### 4. Reynolds-averaged Navier–Stokes models

For several decades, the most popular approach for simulating industrial turbulent flows has been the RANS, where the statistical averaging is based on ensemble averaging (Reynolds 1895). The fundamental approach is to decompose the flow variables into an ensemble mean value component and a fluctuating one, substituting them into the original equations and then ensemble-averaging the resulting equations.

##### 4.1. Reynolds-averaged Navier–Stokes equations

For compressible flows with significant compressibility effects, the averaging is of the Favre type (Smits & Dussauge 2006). Note that we let the reference viscosity equal the dimensional viscosity so that the dimensionless viscosity equals one. The non-dimensional Favre-averaged continuity, momentum and energy equations can be respectively written in conservation form as (Huang *et al.* 1995)

$$\frac{\partial \langle \rho \rangle}{\partial t} + \frac{\partial \langle \rho \rangle \{u_k\}}{\partial x_k} = 0, \tag{4.1}$$

$$\frac{\partial \langle \rho \rangle \{u_i\}}{\partial t} + \frac{\partial \langle \rho \rangle \{u_i\} \{u_k\}}{\partial x_k} = - \frac{\partial \langle p \rangle}{\partial x_i} + \frac{\partial \langle \tau_{ik} \rangle}{\partial x_k} - \frac{\partial \langle \rho \rangle \{u_i'' u_k''\}}{\partial x_k}, \tag{4.2}$$

Assessment of turbulence models using DNS data

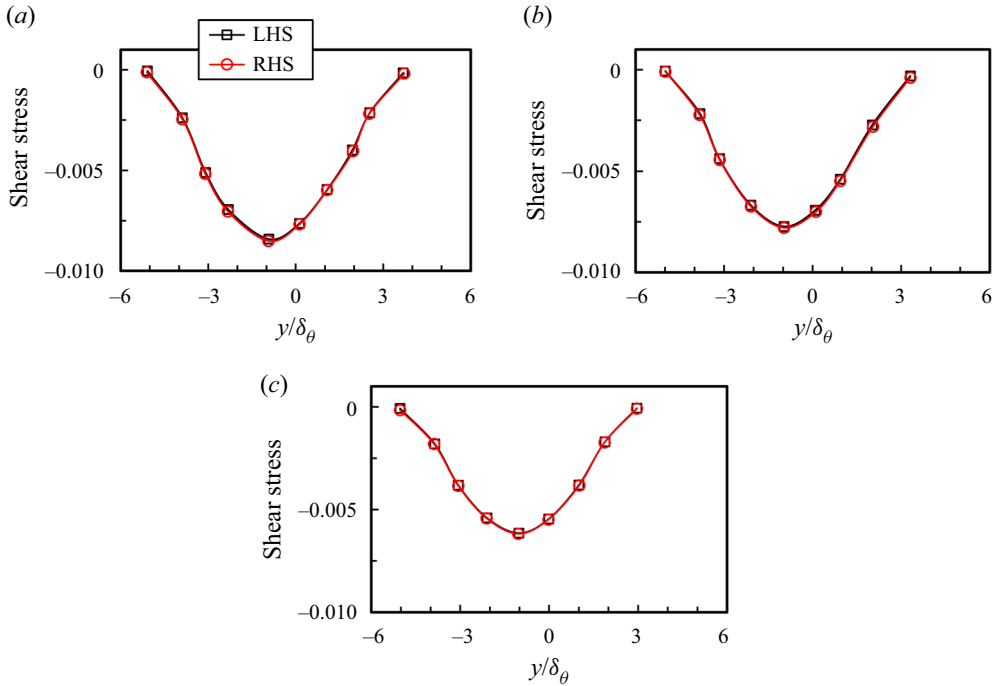


Figure 6. Cross-stream profiles of the left-hand side (black squares) and right-hand side (red circles) of (3.7) for (a)  $M_c = 0.3$ , (b)  $M_c = 0.5$ , and (c)  $M_c = 0.7$ . All terms are extracted at  $x - x_E = 300$  and normalized by  $(\Delta U)^2$ .

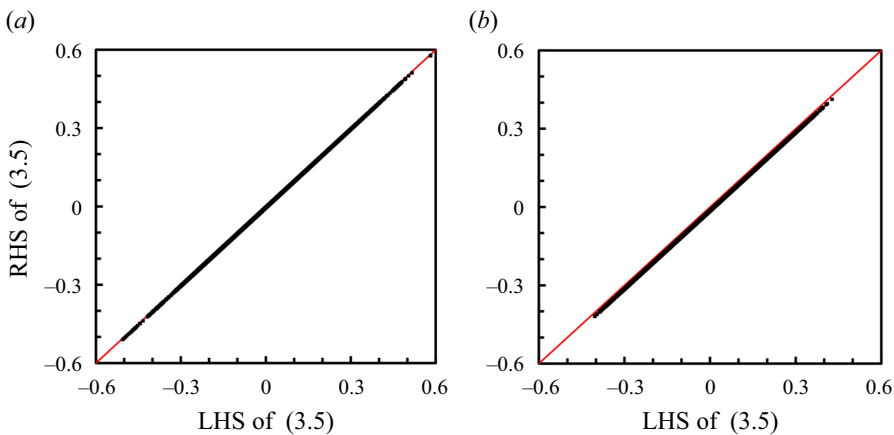


Figure 7. Scatter plots of the normalized Favre streamwise velocity fluctuations obtained by DNS (left-hand side of (3.5)) versus that obtained by the models (right-hand side of (3.5)) for (a)  $M_c = 0.3$  and (b)  $M_c = 0.7$ . All terms are extracted at the centre of the shear layer (see table 2) and normalized by  $(\Delta U)$ . The 45-degree line is shown in red.

$$\begin{aligned} & \frac{\partial}{\partial t} \langle \rho \rangle \left( \frac{\{T\}}{(\gamma - 1)\gamma M_f^2} + \{K\} + \{k\} \right) + \frac{\partial}{\partial x_k} \langle \rho \rangle \{u_k\} \left( \frac{\{T\}}{(\gamma - 1)\gamma M_f^2} + \frac{\langle p \rangle}{\langle \rho \rangle} + \{K\} + \{k\} \right) \\ &= \frac{\partial}{\partial x_k} (\langle \tau_{ik} \rangle \langle u_i \rangle + \langle \tau'_{ik} u'_i \rangle) + \frac{1}{Re_f} \frac{1}{(\gamma - 1)M_f^2 Pr_f} \frac{\partial^2 \langle T \rangle}{\partial x_k^2} \end{aligned}$$

Location	$x - x_E$ (streamwise)	$y/\delta_\theta$ (cross-stream)	$z$ (spanwise)
Upper-edge	300	3.7	40.3
Centre	300	-0.94	40.3
Lower-edge	300	-5.06	40.3

Table 2. Locations where the data are extracted for examinations of (3.5) and (3.6).

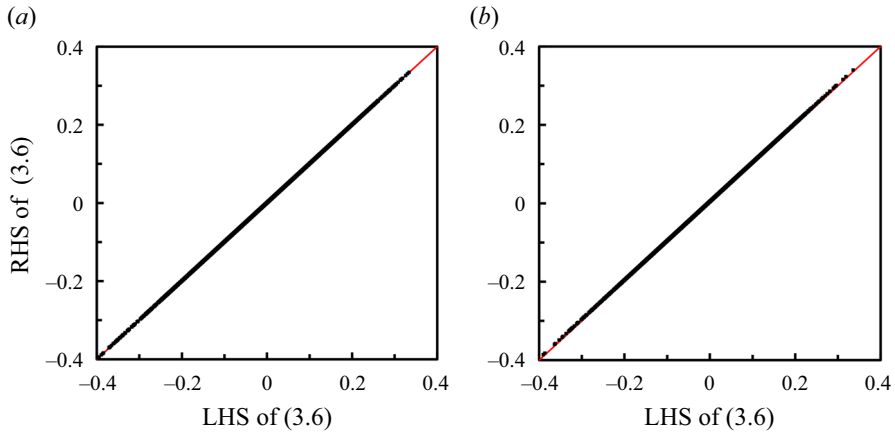


Figure 8. Scatter plots of the normalized Favre cross-stream velocity fluctuations obtained by DNS (left-hand side of (3.6)) versus that computed by the models (right-hand side of (3.6)) for (a)  $M_c = 0.3$  and (b)  $M_c = 0.7$ . All terms are extracted at the centre of the shear layer (see table 2) and normalized by  $(\Delta U)$ . The 45-degree line is shown in red.

$M_c$	Upper edge	Centre	Lower edge
0.3	$6.40 \times 10^{-4}$	$7.87 \times 10^{-3}$	$1.03 \times 10^{-4}$
0.7	$4.89 \times 10^{-3}$	$6.95 \times 10^{-2}$	$1.24 \times 10^{-4}$

Table 3. Comparison of the mean absolute deviation between the left-hand side and right-hand side of (3.5) at various  $M_c$  and different locations. The assessed data are extracted at locations shown in table 2.

$$-\frac{\partial}{\partial x_k} (\langle \rho \rangle \{u_k'' K''\} + \langle \rho \rangle \{u_k'' k''\}) - \frac{1}{(\gamma - 1) M_f^2} \frac{\partial \langle \rho \rangle \{u_k'' T''\}}{\partial x_k}, \tag{4.3}$$

where

$$\{k\} = \frac{1}{2} \{u_i''^2\}, \tag{4.4}$$

$$\{K\} = \frac{1}{2} \{u_i\}^2, \tag{4.5}$$

$$\tau'_{ik} = \frac{1}{Re_f} \left( \frac{\partial u'_i}{\partial x_k} + \frac{\partial u'_k}{\partial x_i} - \frac{2}{3} \frac{\partial u'_l}{\partial x_l} \delta_{ik} \right), \tag{4.6}$$

$M_c$	Upper edge	Centre	Lower edge
0.3	$1.01 \times 10^{-4}$	$2.59 \times 10^{-3}$	$1.37 \times 10^{-5}$
0.7	$1.06 \times 10^{-3}$	$2.45 \times 10^{-2}$	$2.04 \times 10^{-4}$

Table 4. Comparison of the mean absolute deviation between the left-hand side and right-hand side of (3.6) at various  $M_c$  and different locations. The assessed data are extracted at locations presented in table 2.

$$\langle \tau_{ik} \rangle = \frac{1}{Re_f} \left( \frac{\partial \langle u_i \rangle}{\partial x_k} + \frac{\partial \langle u_k \rangle}{\partial x_i} - \frac{2}{3} \frac{\partial \langle u_l \rangle}{\partial x_l} \delta_{ik} \right). \tag{4.7}$$

In (4.3),  $\{K\}$  and  $\{k\}$  are the Favre-averaged mean kinetic energy and the Favre-averaged turbulent kinetic energy, respectively. The turbulent transport,  $\langle \rho \rangle \{u_k'' k''\}$ , and molecular diffusion,  $\langle \tau_{ik}' u_i' \rangle$ , are typically very small (Speziale *et al.* 1991; Wilcox 2006), and thus these terms can be neglected. Models for Reynolds stresses,  $\{u_i'' u_k''\}$ , and the heat flux,  $\{u_k'' T''\}$ , are required to close (4.1)–(4.3) (Wilcox 2006).

The Reynolds stresses,  $R_{ij} = \{u_i'' u_j''\}$ , are the components of the second-order tensor, which is intrinsically symmetric, such that  $R_{ij} = R_{ji}$ . The diagonal components are normal stresses, e.g.  $R_{11}$ ,  $R_{22}$  and  $R_{33}$ . The off-diagonal components are shear stresses, such as  $R_{12}$ ,  $R_{13}$  and  $R_{23}$ . The normalized turbulence intensity in different directions can be represented in terms of Reynolds stresses, e.g.  $\sqrt{R_{ij}}/(\Delta U)$ . Figure 9 presents the cross-stream profiles of normalized turbulence intensities from the current DNS and experiments. The compared data are extracted in the self-similar turbulent region. It can be seen that the magnitudes of  $\sqrt{R_{11}}/(\Delta U)$  and  $\sqrt{|R_{12}|}/(\Delta U)$  of the current simulations agree well with the experimental results from Goebel & Dutton (1991) for  $M_c = 0.46$  and 0.69, while  $\sqrt{R_{33}}/(\Delta U)$  presents good agreement with the experimental result of Gruber, Messersmith & Dutton (1993). The magnitudes of  $\sqrt{R_{22}}/(\Delta U)$  from the present DNS fall between the experimental results from Goebel & Dutton (1991) for  $M_c = 0.2$  and 0.46, and are higher than that by Gruber *et al.* (1993) for  $M_c = 0.8$ . In addition to presenting the cross-stream profiles of turbulence intensities in figure 9, we also tabulate their magnitudes in table 5 for better quantitative comparisons between DNS and experimental results. Particularly note that based on the present DNS results,  $\sqrt{R_{11}}/(\Delta U) > \sqrt{R_{33}}/(\Delta U) > \sqrt{R_{22}}/(\Delta U)$  for all cases with  $M_c = 0.3, 0.5$  and 0.7, which indicates that the fluctuations in this work are strongly three-dimensional.

Reynolds stresses,  $R_{ij}$ , are often used to characterize the flow structure motions. The isotropic stress is defined as  $\frac{2}{3}k\delta_{ij}$ ; the deviatoric anisotropic part is then defined as (Pope 2000)

$$a_{ij} = R_{ij} - \frac{2}{3}k\delta_{ij}. \tag{4.8}$$

The normalized anisotropy tensor, hereinafter referred to as Reynolds stress anisotropy, is defined as

$$b_{ij} = \frac{a_{ij}}{2k} = \frac{R_{ij}}{R_{ll}} - \frac{1}{3}\delta_{ij}. \tag{4.9}$$

Note that in turbulent flows modelling, the Reynolds stress anisotropy tensor  $b_{ij}$  is a significant characteristic of velocity fluctuations (Pantano & Sarkar 2002). In addition, the tensor  $b_{ij}$  is often used to describe the motions of vortex structures (Smyth & Moum 2000).

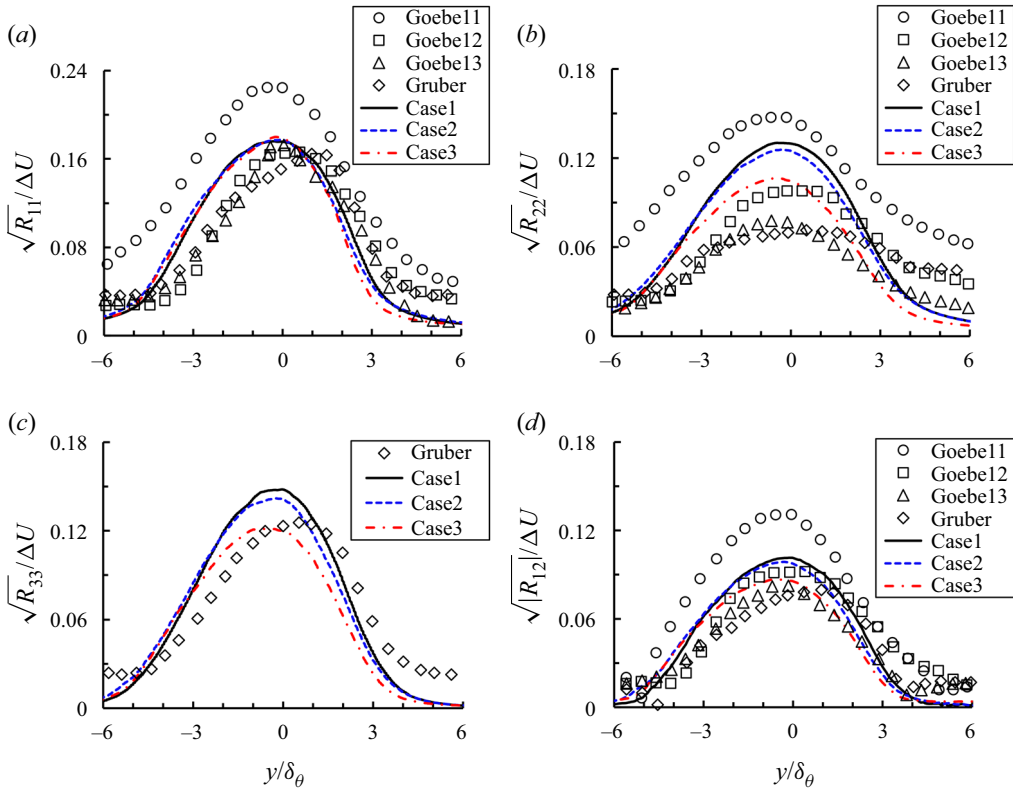


Figure 9. Comparisons of the turbulent intensities, (a)  $\sqrt{R_{11}}/(\Delta U)$ , (b)  $\sqrt{R_{22}}/(\Delta U)$ , (c)  $\sqrt{R_{33}}/(\Delta U)$  and (d)  $\sqrt{|R_{12}|}/(\Delta U)$  in the self-similar turbulent region between the present and experimental results. Goebel1, Goebel2 and Goebel3 represent the results by Goebel & Dutton (1991) for  $M_c = 0.2, 0.46$  and  $0.69$ , respectively. Gruber represents the results by Gruber *et al.* (1993) for  $M_c = 0.8$ . Case1, Case2 and Case3 stand for the present results for  $M_c = 0.3, 0.5$  and  $0.7$ , respectively.

We examine tensor  $b_{ij}$  as a function of the cross-stream coordinate for the self-similar turbulent region. Figure 10 presents comparisons of different components of tensor  $b_{ij}$  for various convective Mach numbers. At the shear layer centre, the magnitude of  $b_{11}$  increases significantly, while the magnitudes of  $b_{22}$  and  $b_{33}$  slightly increase (more negative) with increasing convective Mach number. This different behaviour is attributed to the fact that the values of Reynolds stresses,  $R_{22}$  and  $R_{33}$ , decrease as the convective Mach number increases, while the value of  $R_{11}$  remains almost the same. However, no obvious trend can be found with respect to the effect of compressibility on  $b_{12}$ .

Figure 10(a) shows that the positive values of  $b_{11}$  distribute around the centre and edges of the shear layer owing to the dominance of the streamwise component of the velocity fluctuations at these areas. In contrast, two regions in the cross-stream profile show near zero  $b_{11}$ . One region is laterally above the centre of the shear layer, between the high-speed free-stream and the upper shear layer; another region is laterally below the shear layer, between the low-speed free-stream and the lower shear layer. The value of  $b_{11}$  near zero means the normal Reynolds stress,  $R_{11}$ , is similar in magnitude to the average of  $R_{22}$  and  $R_{33}$ . It indicates that the regions with near zero  $b_{11}$  contain the velocity fluctuations which are similar in different directions. Similar discussions hold true for figures 10(b) and 10(c). Figure 10(d) reveals strong negative  $b_{12}$  at the centre of the shear layer. The strong negative



Turbulence intensity on centreline

$M_c$	$\sqrt{R_{11}}/(\Delta U)$	$\sqrt{R_{22}}/(\Delta U)$	$\sqrt{R_{33}}/(\Delta U)$	$\sqrt{ R_{12} }/(\Delta U)$	Study
0.20	0.224	0.147	–	0.131	Goebel & Dutton (1991)
0.30	0.176	0.130	0.148	0.101	Present DNS
0.46	0.166	0.098	–	0.092	Goebel & Dutton (1991)
0.50	0.177	0.126	0.142	0.099	Present DNS
0.69	0.173	0.078	–	0.082	Goebel & Dutton (1991)
0.70	0.178	0.107	0.121	0.087	Present DNS
0.80	0.164	0.071	0.126	0.080	Gruber <i>et al.</i> (1993)

Table 5. The turbulence intensities on the centreline of the shear layer for different convective Mach numbers in the self-similar turbulent region.

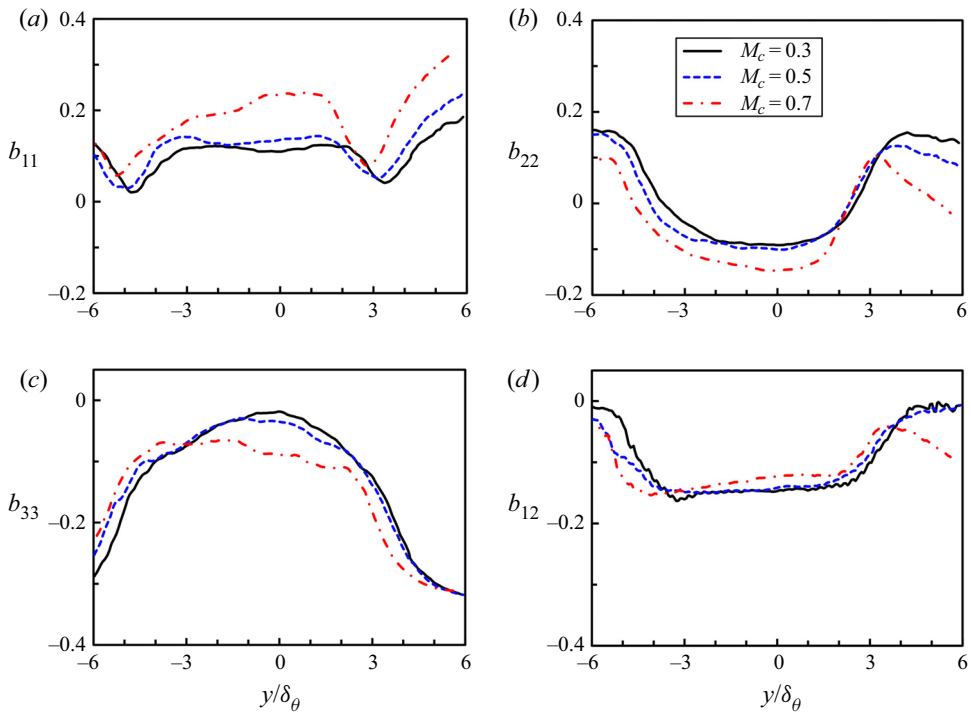


Figure 10. Comparisons of the cross-stream profiles of (a)  $b_{11}$ , (b)  $b_{22}$ , (c)  $b_{33}$  and (d)  $b_{12}$  in self-similar turbulent region for  $M_c = 0.3, 0.5$  and  $0.7$ .

correlation between the streamwise and cross-stream velocity fluctuations indicates that these fluctuations are structured to facilitate the dissipation of energy from the shear layer (Smyth & Moum 2000).

The Reynolds stress anisotropy tensor,  $b_{ij}$ , and the Reynolds stress tensor,  $R_{ij}$ , can be related to each other through

$$R_{ij} = 2k \left( \frac{1}{3} \delta_{ij} + b_{ij} \right). \quad (4.10)$$

In the following, we describe several approaches for determining Reynolds stress tensor,  $R_{ij}$ . The transport equation of the Reynolds stress tensor can be written as (Pantano & Sarkar 2002)

$$\frac{\partial \langle \rho \rangle R_{ij}}{\partial t} + \frac{\partial \langle \rho \rangle \{u_k\} R_{ij}}{\partial x_k} = \langle \rho \rangle \mathcal{P}_{ij} - \frac{\partial T_{ijk}}{\partial x_k} - \langle \rho \rangle \epsilon_{ij} + \Pi_{ij} + \Sigma_{ij}. \quad (4.11)$$

Here, the turbulent production, turbulent transport, turbulent dissipation, pressure–strain correlation and mass flux coupling terms are respectively

$$\mathcal{P}_{ij} = - \left( R_{ik} \frac{\partial \{u_j\}}{\partial x_k} + R_{jk} \frac{\partial \{u_i\}}{\partial x_k} \right), \quad (4.12)$$

$$T_{ijk} = \langle \rho u_i'' u_j'' u_k'' \rangle + \langle p' u_i' \rangle \delta_{jk} + \langle p' u_j' \rangle \delta_{ik} - (\langle \tau_{jk}' u_i'' \rangle + \langle \tau_{ik}' u_j'' \rangle), \quad (4.13)$$

$$\epsilon_{ij} = \frac{1}{\langle \rho \rangle} \left\langle \tau_{jk}' \frac{\partial u_i''}{\partial x_k} + \tau_{ik}' \frac{\partial u_j''}{\partial x_k} \right\rangle, \quad (4.14)$$

$$\Pi_{ij} = \left\langle p' \left( \frac{\partial u_i''}{\partial x_j} + \frac{\partial u_j''}{\partial x_i} \right) \right\rangle, \quad (4.15)$$

$$\Sigma_{ij} = \langle u_i'' \rangle \left( \frac{\partial \langle \tau_{jk} \rangle}{\partial x_k} - \frac{\partial \langle p \rangle}{\partial x_j} \right) + \langle u_j'' \rangle \left( \frac{\partial \langle \tau_{ik} \rangle}{\partial x_k} - \frac{\partial \langle p \rangle}{\partial x_i} \right). \quad (4.16)$$

In the above exact Reynolds stress transport equation, (4.11), the turbulent production term,  $\mathcal{P}_{ij}$ , is exact and does not require modelling because the Reynolds stresses and the mean flow velocity are given by the transport equations. Other terms on the right-hand side of (4.11) need modelling. The pressure–strain correlation,  $\Pi_{ij}$ , is the most important term to be modelled (Cecora *et al.* 2012).

By setting the indices of (4.11) such that  $j = i$ , we can obtain the following transport equation for the turbulent kinetic energy,  $\{k\} = \frac{1}{2} \{u_i''^2\} = \frac{1}{2} R_{ii}$ ,

$$\begin{aligned} \frac{\partial \langle \rho \rangle \{k\}}{\partial t} + \frac{\partial \langle \rho \rangle \{u_k\} \{k\}}{\partial x_k} = & - \langle \rho \rangle \{u_i'' u_k''\} \frac{\partial \{u_i\}}{\partial x_k} - \frac{\partial \langle \rho \rangle \{u_k'' k''\}}{\partial x_k} - \frac{\partial \langle p' u_k' \rangle}{\partial x_k} + \frac{\partial \langle \tau_{ik}' u_i' \rangle}{\partial x_k} \\ & - \left\langle \tau_{ik}' \frac{\partial u_i'}{\partial x_k} \right\rangle - \langle u_k'' \rangle \frac{\partial \langle p \rangle}{\partial x_k} + \langle u_i'' \rangle \frac{\partial \langle \tau_{ik} \rangle}{\partial x_k} + \left\langle p' \frac{\partial u_k'}{\partial x_k} \right\rangle. \end{aligned} \quad (4.17)$$

Based on the literature (Favre 1965, 1969; Lele 1994; Huang *et al.* 1995; Pope 2000), the second term on the left-hand side of (4.17) represents kinetic energy convection. The terms on the right-hand side are, respectively, the turbulent production, turbulent convection, pressure transport, viscous diffusion, turbulent viscous dissipation, enthalpic production, compressibility term resulting from turbulent fluctuations and pressure–dilatation correlation. Note that the last three terms are compressibility related terms arising from turbulent fluctuations.

#### 4.2. Formulations of different RANS models

To improve the model accuracy, researchers take higher and higher moments for models, e.g. from the Boussinesq eddy-viscosity approximation, algebraic (zero-equation) models, one-equation models, two-equation models, four-equation models to Reynolds-stress seven-equation models (Pope 2000). Consequently, we generate additional unknowns at

each level. The purpose of turbulence modelling is to create approximations for the unknowns and finally achieve closure. Most of the compressible turbulence modelling approaches begin with incompressible flows and often provide satisfying results (Smits & Dussauge 2006). In contrast to incompressible flows, no model is able to provide accurate results for high compressible flows.

Among various RANS models, the two-equation  $k-\epsilon$  model is most commonly used in turbulent free shear flows, while the Reynolds-stress model is currently the most comprehensive turbulent modelling approach (Wilcox 2006). For the  $k-\epsilon$  model, several unclosed terms in the turbulent kinetic energy transport equation need to be modelled, such as the turbulent kinetic energy dissipation term, turbulent transport terms and compressibility terms resulting from turbulent fluctuations and pressure–dilatation correlation. The turbulent kinetic energy dissipation term is modelled using the hypothesis of high Reynolds numbers, which means the dissipation is assumed to have the form of isotropic dissipation,  $\epsilon$  (Haase *et al.* 2006). For the modelling of the diffusion terms, the turbulent-transport terms are lumped together and modelled using a classical gradient-diffusion hypothesis (Daly & Harlow 1970). The model constants associated with the diffusion and dissipation terms are either chosen as constants for the whole flow (Schmidt & Schumann 1989) or calculated dynamically (Ghosal *et al.* 1995). To account for the compressibility effect, researchers often model the dilatational dissipation term when simulating compressible flows (Sarkar *et al.* 1989, 1991; Zeman 1990; Wilcox 1992). Additionally, the pressure–dilatation correlation, which is the trace of the pressure–strain correlation tensor, plays a key role in the  $k-\epsilon$  model to mimic the influence of compressibility. The functions of the pressure–dilatation correlation in the  $k-\epsilon$  model are similar to that of the pressure–strain correlation in the Reynolds-stress model (Wilcox 2006).

For the Reynolds-stress model, the unclosed terms in transport equations are turbulent transport terms, dissipation term and pressure–strain correlation. The turbulent transport terms contain contributions of turbulent transport, pressure diffusion and viscous diffusion, where the pressure diffusion term is often considered negligible (Wilcox 1992). As discussed above, the contributions of turbulent transport terms can be combined and approximated using a generalized gradient diffusion model (Daly & Harlow 1970). Moreover, the dissipation term is often modelled by an isotropic tensor,  $\epsilon_{ij} = 2\epsilon/3$ , based on the Kolmogorov hypothesis of local isotropy (Haase *et al.* 2006). An additional transport equation is required to provide the isotropic dissipation term,  $\epsilon$ . Last but not least, the pressure–strain correlation is one of the most important terms in the Reynolds-stress equations for the following reasons. The pressure–strain correlation is mainly responsible for the shear layer growth rate, the turbulence kinetic energy redistribution (Wilcox 2006) and the influence of compressibility (Pope 2000). It also has the same order of magnitude as the production term in the Reynolds-stress equations (see figure 13). In this work, we only consider the assessments of some commonly used dilatational dissipation, pressure–dilatation correlation and pressure–strain correlation models and present them in the following section.

#### 4.2.1. Modelling the dilatational dissipation term

The turbulent dissipation in the turbulent kinetic energy transport equation is also called the scalar dissipation rate,  $\epsilon = \epsilon_{ii}/2 = \langle \tau'_{ik} \partial u'_i / \partial x_k \rangle$ . The quantity,  $\epsilon$ , can be decomposed into the solenoidal dissipation,  $\epsilon_s$ , dilatational dissipation,  $\epsilon_d$ , and inhomogeneous

dissipation,  $\epsilon_I$ : (Huang *et al.* 1995)

$$\epsilon \approx \epsilon_s + \epsilon_d + \epsilon_I, \tag{4.18}$$

where

$$\epsilon_s = \frac{2}{Re_f} \langle \omega'_{ij} \omega'_{ij} \rangle, \quad \text{with } \omega'_{ij} = \frac{1}{2} \left( \frac{\partial u'_i}{\partial x_j} - \frac{\partial u'_j}{\partial x_i} \right), \tag{4.19}$$

$$\epsilon_d = \frac{4}{3Re_f} \left\langle \frac{\partial u'_i}{\partial x_i} \frac{\partial u'_k}{\partial x_k} \right\rangle, \tag{4.20}$$

$$\epsilon_I = \frac{2}{Re_f} \left( \frac{\partial^2 \langle u'_i u'_j \rangle}{\partial x_i \partial x_j} - 2 \frac{\partial}{\partial x_i} \left\langle u'_i \frac{\partial u'_j}{\partial x_j} \right\rangle \right). \tag{4.21}$$

The inhomogeneous dissipation mainly arises from the shear between the wall and the shear layer (Brown *et al.* 2017; Li *et al.* 2021). As expected, the inhomogeneous dissipation is close zero in the turbulence area of the free shear layer (without wall) based on the present DNS data. The inhomogeneous dissipation shows a negligible contribution to the turbulent kinetic energy transport equation in the free shear layer but has a significant contribution in the boundary shear layer (Lele 1994; Huang *et al.* 1995; Brown *et al.* 2017).

In the  $k-\epsilon$  model, the dilatational dissipation term is responsible for the reduction in growth rate as compressibility increases, thus it is a function of turbulent Mach number,  $M_t = \sqrt{k}/c_0$  (Sarkar *et al.* 1989). Here,  $c_0 = (c_1 + c_2)/2$  is the mean speed of sound. Therefore, the magnitude of the dilatational dissipation term increases with increasing turbulent Mach number. Sarkar *et al.* (1989) proposed

$$\epsilon_d = M_t^2 \epsilon_s. \tag{4.22}$$

The study by Zeman (1990) suggested

$$\epsilon_d = 0.75 \left( 1 - \exp \left\{ - \left[ \frac{M_t - 0.1}{0.6} \right]^2 \right\} \right) \epsilon_s. \tag{4.23}$$

Later, Wilcox (1992) introduced

$$\epsilon_d = 1.5 [M_t^2 - 0.1^2] \epsilon_s. \tag{4.24}$$

Figure 11 presents the cross-stream profiles of dilatational dissipation obtained from the present DNS and the models (4.22)–(4.24) for  $M_c = 0.3$  and 0.7. All terms are extracted at  $x - x_E = 300$  and normalized by  $(\Delta U)^3/\delta_\theta$ . It can be seen that all the models unrealistically overpredict the value of the dilatational dissipation, while the model of Zeman (1990) (4.23) shows relatively better agreement than the rest for  $M_c = 0.3$ . In the turbulent kinetic energy transport equation, the dilatational dissipation term converts the turbulent kinetic energy to internal energy. The considered models were primarily devised to increase this energy conversion as the convective Mach number increases to account for the compressibility effects. However, in figure 26(c) of our recently published paper (Li *et al.* 2021), the ratio of the dilatational to solenoidal dissipation reveals that the value of the dilatational dissipation is insignificant compared with the solenoidal dissipation. In summary, the dilatational dissipation is insignificant in the plane free shear flow for the convective Mach numbers considered in this study. Therefore, the models discussed in this paper for dilatational dissipation are unsuitable for compressible plane free shear layer flows for  $M_c \leq 0.7$ .

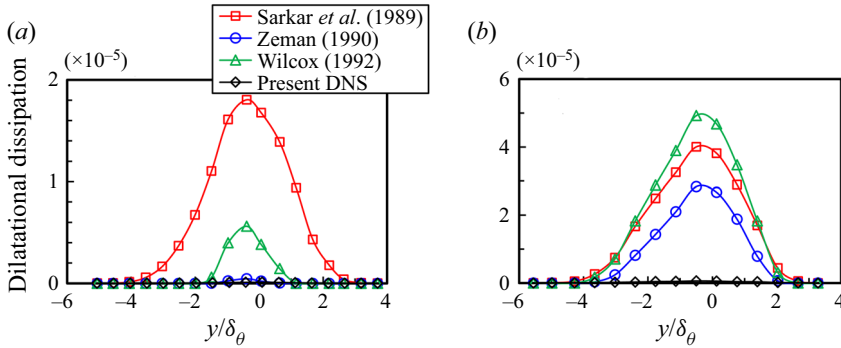


Figure 11. Comparison of dilatational dissipation cross-stream profiles between present DNS and models by Sarkar *et al.* (1989) (4.22), Zeman (1990) (4.23) and Wilcox (1992) (4.24) for (a)  $M_c = 0.3$  and (b)  $M_c = 0.7$ . All terms are extracted at  $x - x_E = 300$  and normalized by  $(\Delta U)^3 / \delta_\theta$ .

#### 4.2.2. Modelling the pressure–dilatation correlation

The pressure–dilatation correlation,  $\Pi = \langle p'(u'_k/x_k) \rangle$ , is intrinsically the trace of the pressure–strain correlation tensor and appears in the turbulent kinetic energy transport equation. Sarkar, Erlebacher & Hussaini (1992), in their  $k-\epsilon$  two-equation model study, suggested that the pressure–dilatation correlation could be related to the turbulent Mach number, the turbulent kinetic energy production,  $\mathcal{P}_{kk} = -\langle \rho \{u'_i u''_k\} \{u_i/x_k\} \rangle$ , and the solenoidal part of the dissipation rate,  $\epsilon_s = (2/Re_f) \langle \omega'_{ij} \omega'_{ij} \rangle$ , i.e.

$$\Pi = -0.15 \langle \rho \rangle \mathcal{P}_{kk} M_t^2 + 0.2 \langle \rho \rangle \epsilon_s M_t^2. \tag{4.25}$$

The purpose of including the turbulent Mach number in the model is to account for the effect of compressibility, which may suppress the growth of the shear layer. Later, El Baz & Launder (1993) proposed a similar model, which involves the divergence of the Favre average velocity,

$$\Pi = 3 \langle \rho \rangle \left( \frac{4}{3} \{k\} \frac{\partial \{u_i\}}{\partial x_i} - \mathcal{P}_{kk} \right) M_t^2. \tag{4.26}$$

Huang *et al.* (1995), based on the study by Sarkar *et al.* (1992), suggested

$$\Pi = -0.4 \langle \rho \rangle \mathcal{P}_{kk} M_t^2 + 0.2 \langle \rho \rangle \epsilon_s M_t^2. \tag{4.27}$$

Figure 12 presents the cross-stream profiles from the DNS and the modelled pressure–dilatation correlation. The corresponding data are extracted from the turbulent section of the shear layer at  $x - x_E = 300$ . The results of the modelled pressure–dilatation correlation are computed from (4.25) (Sarkar *et al.* 1992), (4.26) (El Baz & Launder 1993) and (4.27) (Huang *et al.* 1995) for  $M_c = 0.3$  and 0.7. All these models were mainly designed to decrease the turbulent kinetic energy as the convective Mach number increases to mimic the behaviour of the compressible flow. Based on our previous study (Li *et al.* 2021), we conclude that the pressure–dilatation term’s contribution to the turbulent kinetic energy budget is insignificant even as the convective Mach number is raised to 0.7, which is consistent with the results by Vreman, Sandham & Luo (1996). The authors suggested that the pressure–dilatation correlation is negligible in the turbulent kinetic energy transport equation even at the highest Mach numbers examined. This might arise from the self-cancellation when averaging the instantaneous  $p'(u'_k/x_k)$  over time. Therefore, a reliable model should be able to predict that the pressure–dilatation

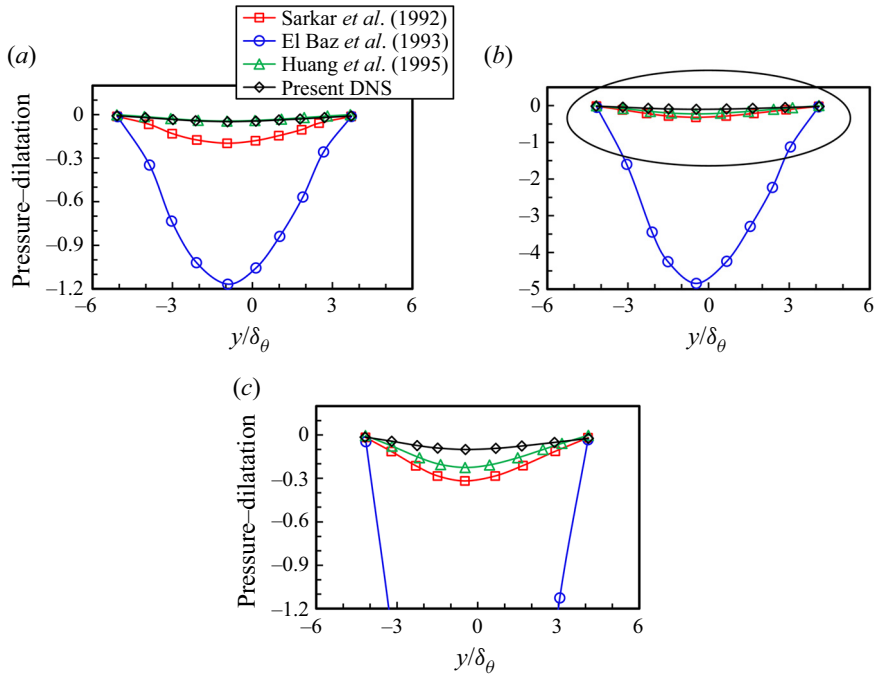


Figure 12. Pressure–dilatation correlation cross-stream profiles generated by the present DNS and models ((4.25), (4.26) and (4.27)) for (a)  $M_c = 0.3$ , (b)  $M_c = 0.7$  and (c) magnified area from panel (b). All terms are extracted at  $x - x_E = 300$  and normalized by  $(\Delta U)^3 / \delta_\theta \times 10^{-4}$ .

correlation is negligible. Unfortunately, [figure 12](#) shows that the models proposed by Sarkar *et al.* (1992) and El Baz & Launder (1993) largely overestimate the magnitude of pressure–dilatation. Thus, these two models are unsuitable for free shear flows with moderate Mach numbers. However, the model proposed by Huang *et al.* (1995) shows exceptional performance for  $M_c = 0.3$  and acceptable prediction for  $M_c = 0.7$ . In conclusion, the model by Huang *et al.* (1995) provides the best prediction, while the model by El Baz & Launder (1993) gives a large overestimate for both  $M_c = 0.3$  and 0.7. Finally, all considered models show more significant discrepancies with the DNS value as the convective Mach number increases from 0.3 to 0.7.

#### 4.2.3. Modelling the pressure–strain correlation

Changes in the pressure–strain correlation components in the Reynolds stress transport equations are responsible for the variations in turbulence structures and free shear layer growth rate (Yoder 2003). The Reynolds stresses decrease with increasing the convective Mach number, but the streamwise normal stress is often less affected (Li *et al.* 2019). The pressure–strain correlation components redistribute the turbulence kinetic energy between the streamwise, cross-stream and spanwise components, which increases the anisotropy of the Reynolds stresses (Wilcox 2006). Hence, to properly account for the variations in Reynolds stresses with increasing convective Mach number, a model capable of predicting the anisotropy of Reynolds stresses is required (Yoder 2003).

The analysis of the transport equations for the Reynolds stress components may help identify the driving factor behind changes of the Reynolds stresses. Different components of production and pressure–strain correlation for  $M_c = 0.3$  and 0.7 are presented in

Assessment of turbulence models using DNS data

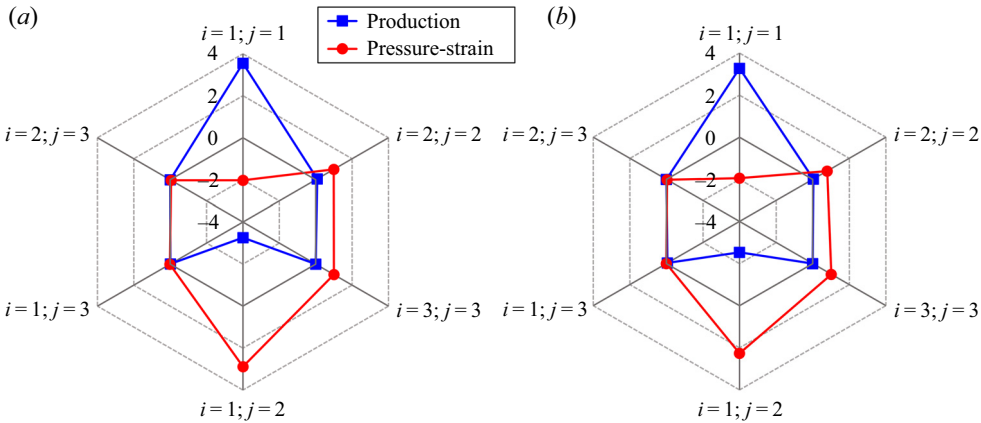


Figure 13. Different components of production and pressure–strain for (a)  $M_c = 0.3$  and (b)  $M_c = 0.7$ . All terms are extracted at  $x - x_E = 300$  and normalized by  $(\Delta U)^3 / \delta_\theta \times 10^{-3}$ .

figure 13. In the streamwise normal stress transport equation ( $i = 1$  and  $j = 1$ ), the production is the dominant source term, while the pressure–strain correlation acts as a sink term. In the cross-stream and spanwise normal stress transport equations ( $i = 2$  and  $j = 2$ ;  $i = 3$  and  $j = 3$ ), however, the production is insignificant and the pressure–strain correlation is the major source term. The shear stress transport equation ( $i = 1$  and  $j = 2$ ) is dominated by the production and pressure–strain correlation terms. In the other shear stress transport equations ( $i = 1$  and  $j = 3$ ;  $i = 2$  and  $j = 3$ ), which involve the shear in the homogeneous direction (spanwise direction), the production and pressure–strain correlation terms appear insignificant. It can be concluded that the pressure–strain correlation term mainly redistributes the turbulence kinetic energy among the normal stresses.

The pressure–strain correlation is one of the essential terms in the Reynolds stress transport equations because it has the same order of magnitude as the turbulent production term (see figure 13). Almost all the pressure–strain correlation models are designed based on the assumption of incompressible and locally homogeneous flows (Yoder 2003). The pressure–strain correlation model devised by Speziale, Sarkar and Gatski (SSG) (Speziale *et al.* 1991) reads

$$\begin{aligned} \Pi_{ij} = & -(C_1 \langle \rho \rangle \epsilon + \frac{1}{2} C_1^* \langle \rho \rangle \mathcal{P}_{kk}) \{a_{ij}\} + C_2 \langle \rho \rangle \epsilon (\{a_{ik}\} \{a_{kj}\} - \frac{1}{3} \{a_{kl}\} \{a_{kl}\} \delta_{ij}) \\ & + (C_3 - C_3^* \sqrt{\{a_{kl}\} \{a_{kl}\}}) \langle \rho \rangle \{k\} \{S_{ij}^*\} \\ & + C_4 \langle \rho \rangle \{k\} (\{a_{ik}\} \{S_{jk}\} + \{a_{jk}\} \{S_{ik}\} - \frac{2}{3} \{a_{kl}\} \{a_{kl}\} \delta_{ij}) \\ & + C_5 \langle \rho \rangle \{k\} (\{a_{ik}\} \{W_{jk}\} + \{a_{jk}\} \{W_{ik}\}). \end{aligned} \tag{4.28}$$

Here,

$$\{a_{ij}\} = \frac{\{R_{ij}\}}{\{k\}} - \frac{2}{3} \delta_{ij} \tag{4.29}$$

is the anisotropy tensor, while

$$\{S_{ij}\} = \frac{1}{2} \left( \frac{\partial \{U_i\}}{\partial x_j} + \frac{\partial \{U_j\}}{\partial x_i} \right) \tag{4.30}$$

and

$$\{S_{ij}^*\} = \{S_{ij}\} - \frac{1}{3}\{S_{kk}\}\delta_{ij} \tag{4.31}$$

are respectively the averaged strain rate and traceless strain rate tensor. Finally,

$$\{W_{ij}\} = \frac{1}{2} \left( \frac{\partial\{U_i\}}{\partial x_j} - \frac{\partial\{U_j\}}{\partial x_i} \right) \tag{4.32}$$

is the averaged rotation rate tensor. The isotropic dissipation rate  $\epsilon$  is provided by an additional transport equation. The model coefficients  $C_1, C_2, C_3, C_4$  and  $C_5$  are 17/10, 21/20, 4/5, 5/8 and 1/5, respectively. The other two coefficients  $C_1^*$  and  $C_3^*$  are set as 9/10 and 65/100, respectively (Speziale *et al.* 1991).

Another pressure–strain correlation model, introduced by Wilcox (2006), is also used to close the six Reynolds stress transport equations. For brevity, we refer to Wilcox pressure–strain correlation model as WilcoxRSM hereafter. The WilcoxRSM is given by

$$\begin{aligned} \Pi_{ij} = & \beta^* \widehat{C}_1 \omega \left( \langle \tau_{ij} \rangle + \frac{2}{3} \{k\} \delta_{ij} \right) - \hat{\alpha} \left( \mathcal{P}_{ij} - \frac{2}{3} \mathcal{P} \delta_{ij} \right) - \hat{\beta} \left( D_{ij} - \frac{2}{3} \mathcal{P} \delta_{ij} \right) \\ & - \hat{\gamma} \{k\} \left( \{S_{ij}\} - \frac{1}{3} \{S_{kk}\} \delta_{ij} \right), \end{aligned} \tag{4.33}$$

with

$$\mathcal{P} = \frac{1}{2} \mathcal{P}_{kk}, \quad \omega = \frac{\epsilon}{C_\mu \{k\}}, \quad D_{ij} = \langle \tau_{ik} \rangle \frac{\partial \{u_k\}}{\partial x_j} + \langle \tau_{jk} \rangle \frac{\partial \{u_k\}}{\partial x_i}. \tag{4.34a-c}$$

The production,  $\mathcal{P}_{ij}$ , from (4.12), and the strain rate tensor,  $\{S_{ij}\}$ , from (4.30), are employed in the SSG and WilcoxRSM models. The closure coefficients  $\beta^*, \widehat{C}_1$  and  $\hat{\alpha}$  are respectively set as 9/100, 9/5 and 181/220, while  $\hat{\beta}, \hat{\gamma}$  and  $C_\mu$  are given as 139/220, 59/55 and 9/100, respectively (Wilcox 2006).

Figure 14 presents the comparison of the cross-stream profiles of DNS and the modelled pressure–strain correlation. All terms are extracted at  $x - x_E = 300$  and normalized by  $(\Delta U)^3 / \delta_\theta$  for  $M_c = 0.3$ . It can be seen from figure 14(a) that the SSG model can roughly predict the sink term, which is the pressure–strain correlation in the streamwise normal stress transport equation ( $i = 1$  and  $j = 1$ ), while the WilcoxRSM model shows excellent estimation. For the cross-stream and spanwise normal stress transport equations ( $i = 2$  and  $j = 2$ ;  $i = 3$  and  $j = 3$ ), the WilcoxRSM model is able to approximately predict the magnitudes of pressure–strain correlation (see figure 14b,c), which acts as the major source term. However, the SSG model underpredicts  $\Pi_{22}$  (significantly) and  $\Pi_{33}$  (slightly).

In contrast, models SSG and WilcoxRSM excellently predict  $\Pi_{12}$  (see figure 14d), which is the dominant term among the six components and has the most significant contribution to the change of Reynolds stresses. The pressure–strain correlation component,  $\Pi_{12}$ , is often used as a primary benchmark to optimize the corresponding models. The last two pressure–strain correlation components,  $\Pi_{13}$  and  $\Pi_{23}$ , show negligible magnitudes compared with the rest of the components owing to the negligible velocity fluctuation gradient that emerged in the homogeneous spanwise direction. These components are insignificant to the change of the Reynolds stresses. However, both the SSG and WilcoxRSM models can accurately predict the value of  $\Pi_{23}$  but considerably overpredict  $\Pi_{13}$ .

The performance of the SSG and WilcoxRSM models in the higher convective Mach number case is shown in figure 15, which compares the modelled pressure–strain



Assessment of turbulence models using DNS data

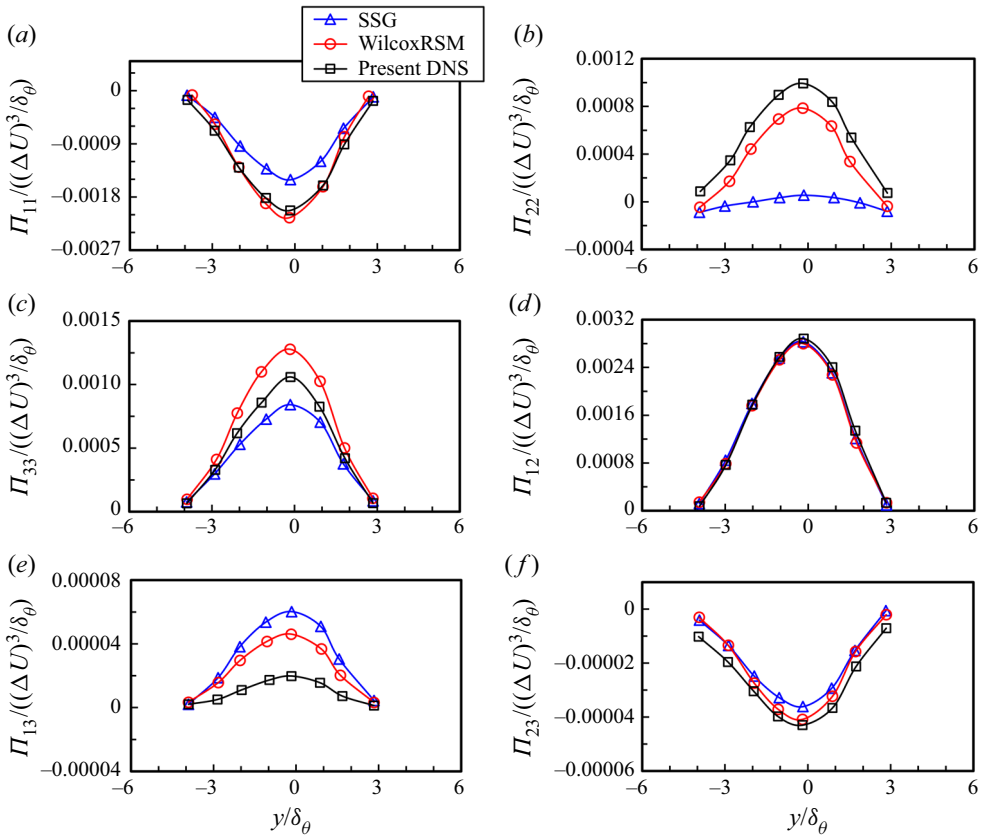


Figure 14. Cross-stream profiles of pressure–strain correlation components (a)  $\Pi_{11}$ , (b)  $\Pi_{22}$ , (c)  $\Pi_{33}$ , (d)  $\Pi_{12}$ , (e)  $\Pi_{13}$  and (f)  $\Pi_{23}$  computed by models and DNS for  $M_c = 0.3$ . All terms are extracted at  $x - x_E = 300$  and normalized by  $(\Delta U)^3 / \delta_\theta$ .

correlation profiles with the present DNS results for  $M_c = 0.7$ . Comparing the performance in the case with  $M_c = 0.3$ , the SSG and WilcoxRSM models show slightly better agreement with the DNS results for components  $\Pi_{11}$ ,  $\Pi_{22}$  and  $\Pi_{33}$  (see figure 15a–c), while show similar agreements for  $\Pi_{12}$  (see figure 15d). However, components  $\Pi_{13}$  and  $\Pi_{23}$ , which are the insignificant ones, are respectively overpredicted and underpredicted by both models. In general, both models can accurately estimate the significant pressure–strain correlation components for  $M_c = 0.3$  and  $0.7$ , even better for the latter.

To account for the reduction in the pressure fluctuation with increasing Mach number, a turbulence model for the pressure–strain correlation, including compressibility, is derived by Fujiwara, Matsuo & Arakawa (2000), i.e.

$$(\Pi_{ij})_{comp} = f(M_t)(\Pi_{ij})_{incomp}, \tag{4.35}$$

where

$$f(M_t) = 1 - \exp\left(-\frac{C_f}{M_t^2}\right). \tag{4.36}$$

Here,  $C_f$  is taken as 0.02 for a compressible plane free shear layer (Fujiwara *et al.* 2000). The subscripts *comp* and *incomp* indicate compressible and incompressible, respectively.

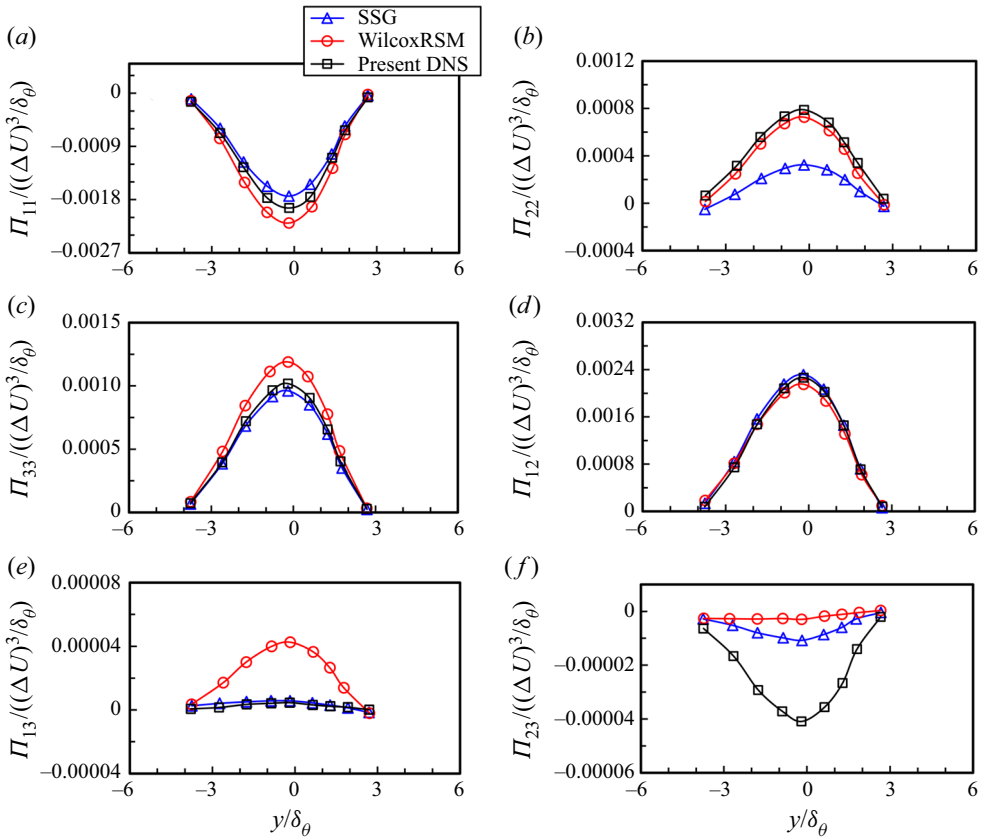


Figure 15. Cross-stream profiles of pressure–strain correlation components (a)  $\Pi_{11}$ , (b)  $\Pi_{22}$ , (c)  $\Pi_{33}$ , (d)  $\Pi_{12}$ , (e)  $\Pi_{13}$  and (f)  $\Pi_{23}$  computed by models and DNS for  $M_c = 0.7$ . All terms are extracted at  $x - x_E = 300$  and normalized by  $(\Delta U)^3/\delta_\theta$ .

In this work, the case with  $M_c = 0.3$  is considered as a reference for the incompressible comparisons owing to the fact that the compressibility effects can be considered negligible for this small convective Mach number (Goebel & Dutton 1991; Pantano & Sarkar 2002). Ideally, the pressure–strain correlation in compressible flow (with  $M_c = 0.7$ ) can be computed using the compressibility modification model by giving the corresponding  $M_t$  and the incompressible pressure–strain correlation (with  $M_c = 0.3$ ). For brevity, we refer to the compressibility modification model of the pressure–strain correlation ( $f(M_t)(\Pi_{ij})_{incomp}$ ) as CMPS.

To examine the viability of the CMPS model, we use this model to calculate the pressure–strain correlation for the case with  $M_c = 0.7$ , then compare with the primitive DNS results, as shown in figure 16. All terms are extracted at  $x - x_E = 300$  and normalized by  $(\Delta U)^3/\delta_\theta$ . It can be seen that CMPS unrealistically underestimates all the components of pressure–strain correlation in the case with  $M_c = 0.7$ , except for the component  $\Pi_{13}$ , which is insignificant in the corresponding Reynolds stress transport equation (discussed previously). In summary, the use of the damping function appears to be somewhat unphysical. This compressibility modification model features a dramatic decrease in the magnitude of the pressure–strain correlation. It is suggested that the compressibility effect is caused by suppressing both the pressure–strain correlation and the turbulence

## Assessment of turbulence models using DNS data

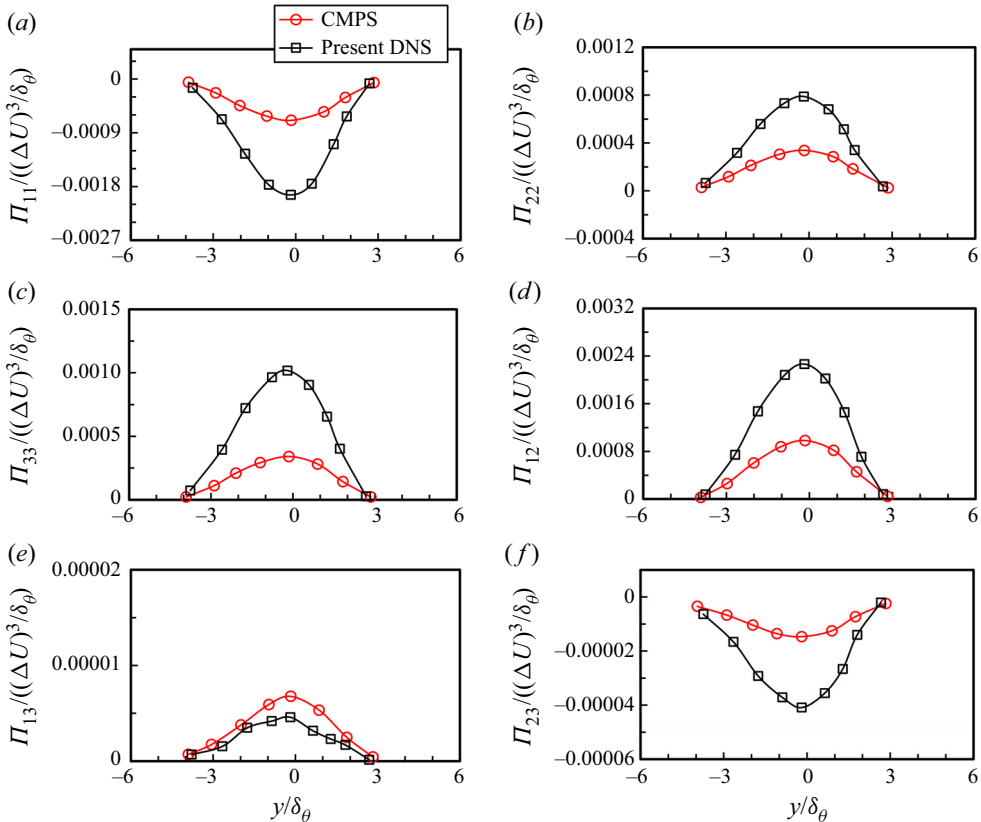


Figure 16. Cross-stream profiles of pressure–strain correlation components (a)  $\Pi_{11}$ , (b)  $\Pi_{22}$ , (c)  $\Pi_{33}$ , (d)  $\Pi_{12}$ , (e)  $\Pi_{13}$  and (f)  $\Pi_{23}$  computed by CMPS ( $f(M_t)(\Pi_{ij})_{incomp}$ ) for  $M_c = 0.7$ . Results from the model are compared with the corresponding DNS ( $M_c = 0.7$ ). All terms are extracted from the turbulent region at  $x - x_E = 300$  and normalized by  $(\Delta U)^3/\delta_\theta$ .

anisotropy (Yoder 2003; Cecora *et al.* 2012). In that case, the turbulent closure problem becomes much more complicated than the simple damping function approach because the pressure–strain correlation models relate to the second-order terms instead of the scalar terms.

### 5. Large-eddy simulation models

The DNS data provides the possibility to investigate the robustness of the SGS modelling. This paper only presents the *a priori* test, using the DNS data of the spatially developing compressible plane free shear layer. Large-eddy simulation is based on the decomposition of a flow variable into resolved and SGS terms (Gullbrand & Chow 2003). To decompose a flow variable, a filtering length scale,  $\Delta$ , is required and is defined as

$$\Delta = (\Delta_x \Delta_y \Delta_z)^{1/3}. \quad (5.1)$$

Here,  $\Delta_x$ ,  $\Delta_y$  and  $\Delta_z$  respectively represent the grid sizes in the streamwise, cross-stream and spanwise directions. If the eddy size is larger than  $\Delta$ , such an eddy is resolved. If the eddy is smaller than  $\Delta$ , it is modelled (Gullbrand & Chow 2003). In other words, the large-scale structures of the flow is resolved to the grid resolution, while the SGS flow

field and its effects on the resolved flow must be modelled. For example, velocity can be decomposed as (Pope 2000)

$$u_i = \bar{u}_i + u'_i. \tag{5.2}$$

Here,  $\bar{u}_i$  is the filtered velocity and  $u'_i$  is the SGS velocity. In the LES models section or hereafter, the superscript ' indicates the sub-grid scale. Note that the LES decomposition of resolved and SGS velocities should not be confused with the RANS decomposition of mean and fluctuation velocities. The filtered velocity can be written in terms of a convolution integral as (Pope 2000)

$$\bar{u}_i(x, t) = \int_{\Omega} u_i(\zeta, t)G(x - \zeta) d\zeta, \tag{5.3}$$

where  $\zeta$  is the dummy variable,  $G$  indicates the filter kernel for the flow field and  $\Omega$  denotes the computational domain. The Favre filtering operation is often applied for compressible turbulence (Favre 1983), i.e.

$$\tilde{u}_i = \frac{\overline{\rho u_i}}{\bar{\rho}}, \tag{5.4}$$

where the overbar and tilde denote the Reynolds and Favre filtering operations, respectively. Before writing the LES equations, the LES filtering properties should be defined. Unlike RANS averaging, in LES (Ghosal & Moin 1995),

$$\bar{\bar{f}} \neq \bar{f} \quad \text{and} \quad \bar{f}' \neq 0, \tag{5.5a,b}$$

where  $f$  is any flow variable. It indicates that averaging a flow field a second time can not reproduce the original averaged flow field.

The filtering method used in this work is nodal filtering (Ghiasi *et al.* 2019). To obtain a filtered value of a variable with a polynomial order  $\zeta$ , we first interpolate the variable to a grid with a lower-polynomial order  $\zeta'$  such that  $\zeta' < \zeta$ . The resulting value is then projected back onto the original grid with the polynomial order of  $\zeta$  (Bouffanais *et al.* 2006). The nodal filter is also called an interpolant-projection filter (Ghiasi *et al.* 2019). This filter functions as a dampener that reduces high-frequency oscillations caused by the  $N_f$  highest-frequency modes in the computational domain. Here,  $N_f = \zeta - \zeta'$  is the filter strength, which is conceptually equivalent to the filtering length scale mentioned previously (see the study by Ghiasi *et al.* (2019) for a detailed description of the nodal filtering in the context of the spectral element method). In this paper, we use  $N_f = 2$  as the first filter length scale and  $N_f = 3$  as the second one. Note that the DNS was conducted using a polynomial order  $\zeta = 5$ .

Filtering the Navier–Stokes equations yields the following filtered conservation equations (Vreman *et al.* 1997):

$$\frac{\partial \bar{\rho}}{\partial t} + \frac{\partial(\bar{\rho}\tilde{u}_j)}{\partial x_j} = 0, \tag{5.6}$$

$$\frac{\partial(\bar{\rho}\tilde{u}_i)}{\partial t} + \frac{\partial(\bar{\rho}\tilde{u}_i\tilde{u}_j)}{\partial x_j} = -\frac{\partial \bar{p}}{\partial x_j} - \frac{\partial \tau_{ij}^{sgs}}{\partial x_j} + \frac{\partial \bar{\sigma}_{ij}}{\partial x_j}. \tag{5.7}$$

In this paper, we only consider modelling the SGS term in the momentum equation. The exact SGS stress tensor,  $\tau_{ij}^{sgs}$  in (5.7), can be expressed as (Vreman *et al.* 1997)

$$\tau_{ij}^{sgs} = \bar{\rho}(\tilde{u}_i\tilde{u}_j - \tilde{u}_i\tilde{u}_j). \tag{5.8}$$

As can be seen, the correlation term,  $\widetilde{u_i u_j}$ , cannot be obtained from the resolved flow field. The unresolved SGS stress tensor  $\tau_{ij}^{sgs}$  needs to be modelled to close the equations system. Leonard (1975) decomposed  $\tau_{ij}^{sgs}$  into three parts: the Leonard stress,  $L_{ij}^M$ , the cross-SGS stress,  $C_{ij}^M$ , and the Reynolds SGS stress,  $R_{ij}^M$ , i.e.

$$\tau_{ij}^{sgs} = L_{ij}^M + C_{ij}^M + R_{ij}^M, \tag{5.9}$$

where

$$L_{ij}^M = \bar{\rho}(\widetilde{u_i u_j} - \widetilde{u_i} \widetilde{u_j}), \tag{5.10}$$

$$C_{ij}^M = \bar{\rho}(\widetilde{u_i u'_j} + \widetilde{u'_i u_j} - \widetilde{u_i} \widetilde{u'_j} - \widetilde{u'_i} \widetilde{u_j}), \tag{5.11}$$

$$R_{ij}^M = \bar{\rho}(\widetilde{u'_i u'_j} - \widetilde{u'_i} \widetilde{u'_j}). \tag{5.12}$$

From the resolved velocity field,  $\tilde{u}$ , Leonard stress components,  $L_{ij}^M$ , can be directly calculated. Leonard stress is often called the outscatter term because the formulation of Leonard stress represents the interaction of two resolved scale structures and such interaction generates small-scale structures. The cross-SGS stress components,  $C_{ij}^M$ , represent the interaction and turbulence energy exchange between large-scale structures and small-scale ones, respectively. However, the net energy exchange is from the large-scale structures to small-scale ones. The Reynolds SGS stress components,  $R_{ij}^M$ , represent the interaction between two SGS stresses and such interaction yields a large-scale structure. This behaviour is also called the backscatter. In contrast to  $C_{ij}^M$ , the  $R_{ij}^M$  only converts turbulent energy from the small-scale structures to the large-scale ones (Xu 2003). Traditionally, researchers separately modelled the Leonard stress, cross-SGS stress and Reynolds SGS stress. However, Speziale (1985) suggested that modelling the three stresses together can also satisfy the Galilean invariance property.

Piomelli *et al.* (1991) proposed that the energy transfer between resolved and SGS structures can be represented by the SGS dissipation, i.e.

$$(\epsilon_{SGS})_{ij} = \tau_{ij}^{sgs} \tilde{S}_{ij}, \tag{5.13}$$

where

$$\tilde{S}_{ij} = \frac{1}{2} \left( \frac{\partial \tilde{u}_i}{\partial x_j} + \frac{\partial \tilde{u}_j}{\partial x_i} \right). \tag{5.14}$$

If  $\epsilon_{SGS}$  is negative, the SGS structures remove energy from the resolved scale structures (forward scatter); if  $\epsilon_{SGS}$  is positive, SGS structures transfer energy to the resolved scale structures (backscatter). The forward and backward scatters of  $(\epsilon_{SGS})_{ij}$  respectively indicated by  $(\epsilon_{ij})_-$  and  $(\epsilon_{ij})_+$ , are defined as (Piomelli *et al.* 1991)

$$(\epsilon_{ij})_- = \frac{1}{2} ((\epsilon_{SGS})_{ij} - |(\epsilon_{SGS})_{ij}|), \tag{5.15}$$

and

$$(\epsilon_{ij})_+ = \frac{1}{2} ((\epsilon_{SGS})_{ij} + |(\epsilon_{SGS})_{ij}|). \tag{5.16}$$

Figure 17 illustrates the normalized  $(\epsilon_{SGS})_{11}$ ,  $(\epsilon_{SGS})_{22}$ ,  $(\epsilon_{SGS})_{33}$ ,  $(\epsilon_{SGS})_{12}$ ,  $(\epsilon_{SGS})_{13}$  and  $(\epsilon_{SGS})_{23}$ , which are computed from the current DNS data for  $M_c = 0.3$ . The contours in red indicate backscatter, while areas in blue indicate forward scatter (absolute dissipation). It can be seen that all components of SGS dissipation contribute both backward and forward scatter in the vortex structure regions. It indicates that energy actively exchanges between small- and large-scale vortex structures in the shear layer.

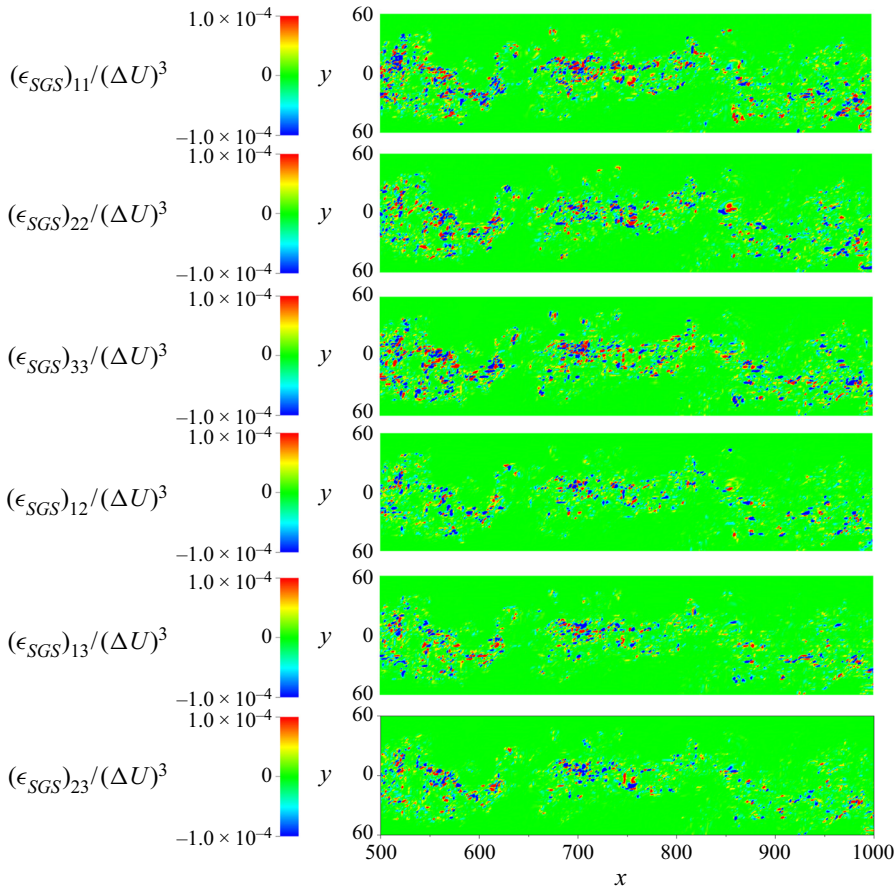


Figure 17. Contours of instantaneous SGS dissipation components,  $(\epsilon_{SGS})_{11}$ ,  $(\epsilon_{SGS})_{22}$ ,  $(\epsilon_{SGS})_{33}$ ,  $(\epsilon_{SGS})_{12}$ ,  $(\epsilon_{SGS})_{13}$  and  $(\epsilon_{SGS})_{23}$  computed from DNS data for  $M_c = 0.3$ . All components are extracted in the turbulent region and normalized by  $(\Delta U)^3$ .

### 5.1. SGS modelling

Most of the LES formulations require SGS stress modelling, and such models are often referred to as SGS models. The SGS models are theoretically simpler and more general than the RANS models because nearly all SGS models are devised for small-scale structures, and the small-scale structures are more isotropic and thus more universal for various flows (Xu 2003). We consider four SGS models in this study: the Smagorinsky model (SM), the dynamic Smagorinsky model (DS), the scale similarity model (SS) and the gradient model (GM). The first two models are eddy viscosity type models. The last two models, SS and GM, function as their names suggest, relevant to structure similarity and velocity gradient concepts.

#### 5.1.1. Smagorinsky model

The first practical SGS model is the Smagorinsky model (SM) (Smagorinsky 1963), based on the methodology of the eddy viscosity model:

$$\tau_{ij}^{sgs} - \frac{1}{3}\tau_{kk}^{sgs}\delta_{ij} = -2\nu_t(\tilde{S}_{ij} - \frac{1}{3}\tilde{S}_{kk}\delta_{ij}), \quad (5.17)$$

where  $\tau_{kk}^{sgs}$  is the isotropic part of  $\tau_{ij}^{sgs}$  and  $\nu_t$  is the eddy viscosity. The eddy viscosity is defined as (Smagorinsky 1963)

$$\nu_t = (C_t \Delta)^2 \bar{\rho} |\tilde{S}|, \quad (5.18)$$

where the magnitude of the strain rate tensor is

$$|\tilde{S}| = (2\tilde{S}_{mn}\tilde{S}_{mn})^{1/2}. \quad (5.19)$$

Here,  $C_t$  is the Smagorinsky coefficient and is set as a constant.

The Smagorinsky model assumes a proportional relation between the SGS stress tensor and the strain rate tensor. This model, applying the gradient diffusion methodology, is similar to the Boussinesq approximation for RANS models. The coefficient,  $C_t$ , can be estimated by analysing the isotropic turbulence decay (Smagorinsky 1963). However, there are many unavoidable limitations when using the Smagorinsky model. The value of  $C_t$  must be varied for different types of flows (Moin *et al.* 1991). For example, Lilly (1966) proposed  $C_t = 0.23$  in the homogeneous isotropic turbulence, while Deardroff (1970) suggested  $C_t = 0.1$  for a turbulent channel flow. This paper evaluates the Smagorinsky model using the latter value of 0.1 suggested by Deardroff (1970). Moreover, the viscous dissipation would not vanish in the laminar region (Moin *et al.* 1991). Instead, the model would overly dissipate energy in the laminar region and the transition region (Piomelli & Zang 1991). Finally, a well-known limitation of this model is that it cannot account for energy backscatter (Moin *et al.* 1991), which is the process where the turbulent energy transfers from small-scale structures back to large-scale ones.

### 5.1.2. Dynamic eddy viscosity model

The dynamic eddy viscosity model (DM) (Germano *et al.* 1991) functions as an eddy viscosity model but with a dynamic Smagorinsky coefficient. The dynamic coefficient is obtained based on the scale similarity concepts. This model computes the coefficient both spatially and temporally by using the information in the resolved flow field through two different filter lengths (Xu 2003). Therefore, the coefficient is a function of both space and time. Theoretically, the issue of over dissipation in the laminar and transition regions can be addressed by using this model. The dynamic eddy viscosity model by Moin *et al.* (1991) is considered in this paper. This model inherits the Smagorinsky model, while a dynamic coefficient of  $C_d$  replaces the square of the constant coefficient  $C_t$ :

$$\tau_{ij}^{sgs} - \frac{1}{3}\tau_{kk}^{sgs}\delta_{ij} = -2C_d\Delta^2\bar{\rho}|\tilde{S}|(\tilde{S}_{ij} - \frac{1}{3}\tilde{S}_{kk}\delta_{ij}). \quad (5.20)$$

The Favre filtered SGS stress expression (exact solution) is

$$\tau_{ij}^{sgs} = \bar{\rho}(\widetilde{u_i u_j} - \widetilde{u_i} \widetilde{u_j}) = \overline{\rho u_i u_j} - \frac{\overline{\rho u_i \rho u_j}}{\bar{\rho}}. \quad (5.21)$$

A test filter is introduced in the dynamic model to bring the information from the resolved field (Germano *et al.* 1991). The test filter width,  $\hat{\Delta}$ , with a larger filter length than the resolved grid filter, is defined similarly as the grid filter width. Applying the test filter to

$\tau_{ij}^{sgs}$ , the mentioned Favre filtered SGS stress expression (5.21) becomes

$$\hat{\tau}_{ij}^{sgs} = \widehat{\rho u_i u_j} - \frac{\widehat{\rho u_i \rho u_j}}{\hat{\rho}}. \quad (5.22)$$

The test filtered stress  $T_{ij}$  is defined similarly as the Favre filtered SGS stress expression (5.21)

$$T_{ij} = \widehat{\rho u_i u_j} - \frac{\widehat{\rho u_i} \widehat{\rho u_j}}{\hat{\rho}} \quad (5.23)$$

and is modelled as

$$T_{ij} - \frac{1}{3} T_{kk} \delta_{ij} = -2C_d \hat{\Delta}^2 \hat{\rho} |\hat{S}| (\hat{S}_{ij} - \frac{1}{3} \hat{S}_{kk} \delta_{ij}). \quad (5.24)$$

According to Germano's identity (Germano *et al.* 1991), the relation among  $\tau_{ij}^{sgs}$ ,  $T_{ij}$  and  $L_{ij}$  gives

$$L_{ij} = T_{ij} - \hat{\tau}_{ij}^{sgs} = \frac{\widehat{\rho u_i \rho u_j}}{\hat{\rho}} - \frac{\widehat{\rho u_i} \widehat{\rho u_j}}{\hat{\rho}} = \widehat{\rho \tilde{u}_i \tilde{u}_j} - \frac{\widehat{\rho u_i} \widehat{\rho u_j}}{\hat{\rho}}. \quad (5.25)$$

Substituting equations (5.20) and (5.24) into (5.25) yields

$$L_{ij} = C_d [-2 \hat{\Delta}^2 \hat{\rho} |\hat{S}| (\hat{S}_{ij} - \frac{1}{3} \hat{S}_{kk} \delta_{ij}) + 2 \Delta^2 \bar{\rho} |\tilde{S}| (\tilde{S}_{ij} - \frac{1}{3} \tilde{S}_{kk} \delta_{ij})] = C_d M_{ij}, \quad (5.26)$$

by neglecting the isotropic part of SGS stress tensors  $-\tau_{kk}^{sgs}$  and  $T_{kk}$ . This is because  $\tau_{kk}^{sgs}$  and  $T_{kk}$  are not only negligible in terms of their magnitudes but also destabilize the simulation (Moin *et al.* 1991; Vreman, Geurts & Kuerten 1995b).

Applying the least-squares proposed by Lilly (1992) and spatial averaging, the dynamic coefficient  $C_d$  is defined as

$$C_d = \frac{\langle L_{ij} M_{ij} \rangle}{\langle L_{kl} M_{kl} \rangle}, \quad (5.27)$$

where  $\langle \rangle$  indicates the spatial averaging over the homogeneous direction (spanwise direction in this paper) of the flow.

### 5.1.3. Scale similarity model

In LES, backscatter, which does not exist in eddy viscosity models but is an essential feature of SGS stresses, transfers turbulent energy from small-scale structures back to large-scale ones (Bardina, Ferziger & Reynolds 1980). To reproduce such backscatter, Bardina *et al.* (1980) introduced the first scale similarity model (SS). This model assumes that the structures of different levels of SGS stresses are similar to the smallest resolved stresses. In other words, the SGS stresses can be predicted based on the resolved flow field. This work examines a modified version of the scale similarity model (Speziale 1985)

$$\tau_{ij}^{sgs} \approx C_L \bar{\rho} (\tilde{u}_i \tilde{u}_j - \tilde{u}_i \tilde{u}_j) = C_L L_{ij}^M, \quad (5.28)$$



where  $C_L$  is a similarity coefficient and chosen as unity (Speziale 1985). Here,  $L_{ij}^M$  is the modified Leonard stress defined in (5.10). Based on the definition, the implementation of the scale similarity model requires second filtering (test filtering) on the resolved flow field.

#### 5.1.4. Gradient model

The Gradient model (GM) relates the SGS stress tensor to the inner product of velocity gradients (Clark *et al.* 1979; Vreman *et al.* 1997)

$$\tau_{ij}^{sgs} \approx \frac{\Delta^2}{12} G_{ij}, \tag{5.29}$$

where

$$G_{ij} = \frac{\partial \tilde{u}_i}{\partial x_k} \frac{\partial \tilde{u}_j}{\partial x_k}. \tag{5.30}$$

The gradient model is efficient in terms of computational cost owing to its zero-equation nature. Additionally, the velocity derivatives can be reused in the viscous stresses computations (Vreman *et al.* 1997). However, using this model to close the LES momentum equation may result in a negative viscosity (Leonard 1997) and may cause instabilities.

### 5.2. Comparison with filtered DNS data

The performance of the considered SGS models is studied via the analyses of the correlation coefficient and discrete  $L_2$ -norm. The correlation coefficient,  $R(a, b)$ , and discrete  $L_2$ -norm,  $\|a - b\|_2$ , between two variables ( $a$  and  $b$ ) are respectively defined as (Wright 1921; Liu, Meneveau & Katz 1994; Okong'o & Bellan 2004)

$$R(a, b) = \frac{n \sum_{i=1}^n a_i b_i - \sum_{i=1}^n a_i \sum_{i=1}^n b_i}{\sqrt{\left[ n \sum_{i=1}^n a_i^2 - \left( \sum_{i=1}^n a_i \right)^2 \right] \left[ n \sum_{i=1}^n b_i^2 - \left( \sum_{i=1}^n b_i \right)^2 \right]}}, \tag{5.31}$$

and

$$\|a - b\|_2 = \sqrt{\sum_{i=1}^n (a_i - b_i)^2}, \tag{5.32}$$

where  $a$  and  $b$  are two arbitrary variables, while  $n$  is the number of paired samples. Hereafter,  $R$  represents the correlation coefficient defined by (5.31). The correlation coefficient between the modelled and exact stresses reveals the quality of the modelled spatial structure of the turbulence. The magnitude of  $R$  ranges from 0 to 1. Magnitudes near unity represent a high correlation (Lu, Rutland & Smith 2007). Moreover, the  $L_2$ -norm of the difference between the modelled and exact stresses indicates whether the model accurately predicts the average value of the stress. To better present the  $L_2$ -norm of the difference between the modelled and exact stresses, we normalize it with the  $L_2$ -norm of the exact stress. A normalized  $L_2$ -norm with a significantly less than unity magnitude represents a low relative error.

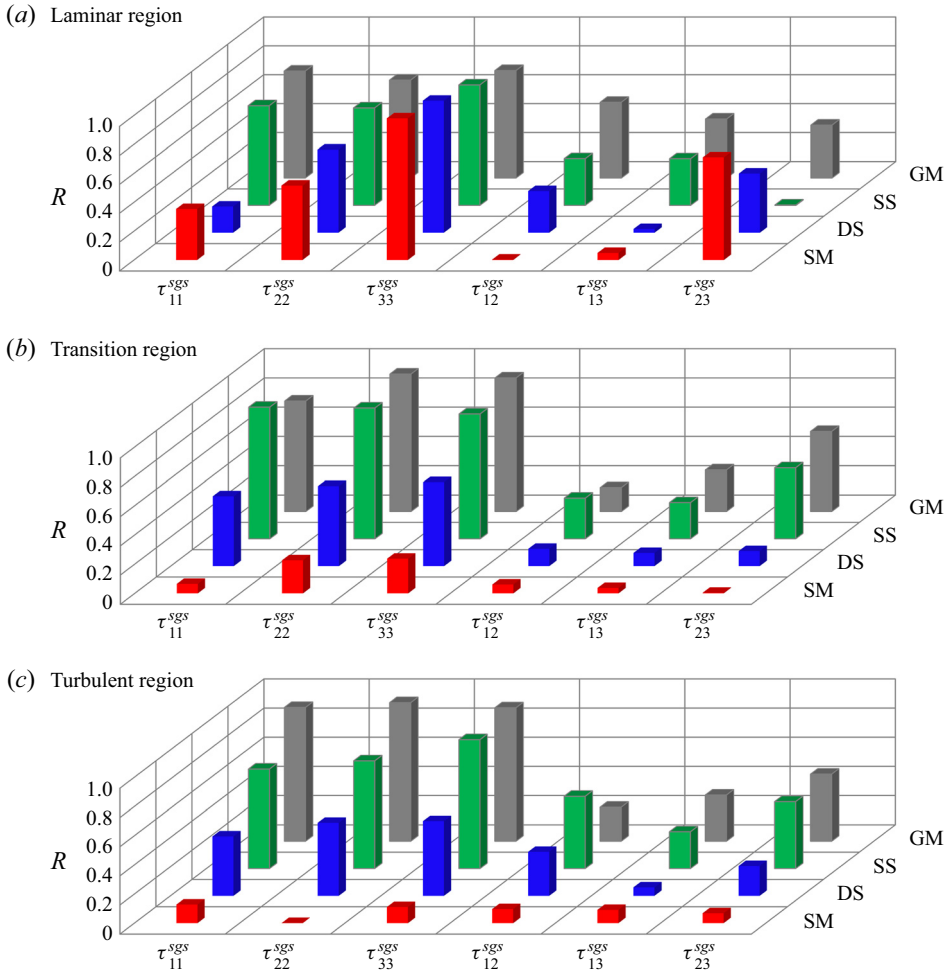


Figure 18. Correlation coefficient,  $R$ , between the exact and the modelled  $\tau_{ij}^{sgs}$  at the (a) laminar region, (b) transition region and (c) turbulent region for  $M_c = 0.3$ .

Owing to the large difference in the behaviours of laminar and turbulent flows, we separately investigate the performance of the SGS models in the laminar, transition and turbulent regions. Based on our previous work (Li *et al.* 2019) for  $M_c = 0.3$  and 0.7, the transition approximately starts at 30 and 230, while the turbulence roughly initiates at 340 and 670, respectively (see table 1).

### 5.2.1. Correlation coefficient

The correlation coefficients,  $R_{ij}$ , between the modelled SGS stress components and the corresponding DNS results are presented in figure 18 for the case with  $M_c = 0.3$ . The considered models include SM, DS, SS and GM. It can be seen that the models can provide high correlations for most of the SGS stress components in the laminar region, except model SM for  $\tau_{12}^{sgs}$  and  $\tau_{13}^{sgs}$ , DS for  $\tau_{13}^{sgs}$  and SS for  $\tau_{23}^{sgs}$ , which give low correlations. However, model GM, in general, shows high correlations for all of the SGS stress components. This arises from the fact that the inner product of velocity gradients in the

## Assessment of turbulence models using DNS data

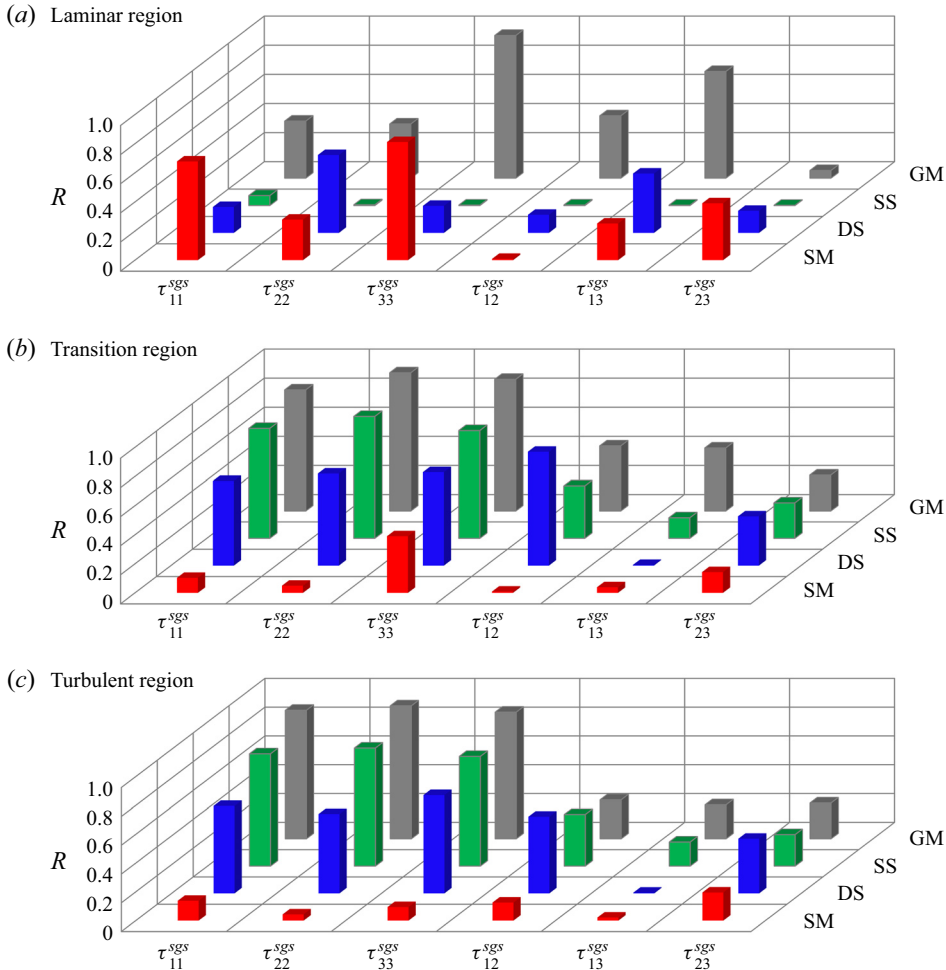


Figure 19. Correlation coefficient,  $R$ , between the exact and the modelled  $\tau_{ij}^{sgs}$  at the (a) laminar region, (b) transition region and (c) turbulent region for  $M_c = 0.7$ .

laminar region is near-zero. It is well known that the SGS model may overly dissipate energy in the laminar region (Piomelli & Zang 1991). The operation of any SGS model should be ideally suspended in the laminar region owing to the absence of small-scale structures.

For the transition region, we can observe an apparent trend that the correlation increases from model SM, DS, SS to GM, except for  $\tau_{11}^{sgs}$  and  $\tau_{12}^{sgs}$ , where there is a small decrease from model SS to GM. For the three normal stresses, the correlations of models SS and GM are higher than 0.9, which implies that models SS and GM can accurately predict the structures of the SGS stress tensor. This is because both models are designed based on the concept that the SGS stresses are approximated from the resolved flow field.

For the most important region in the computational domain, the turbulent region, models SS and GM give high correlations for most SGS stress components. The trend of increasing correlation from model SM, DS, SS to GM, found in the transition region, is also observed in the turbulent region. In general, the model GM shows the highest correlation compared with the rest, while model SM gives the worst performance. The reasons might be the

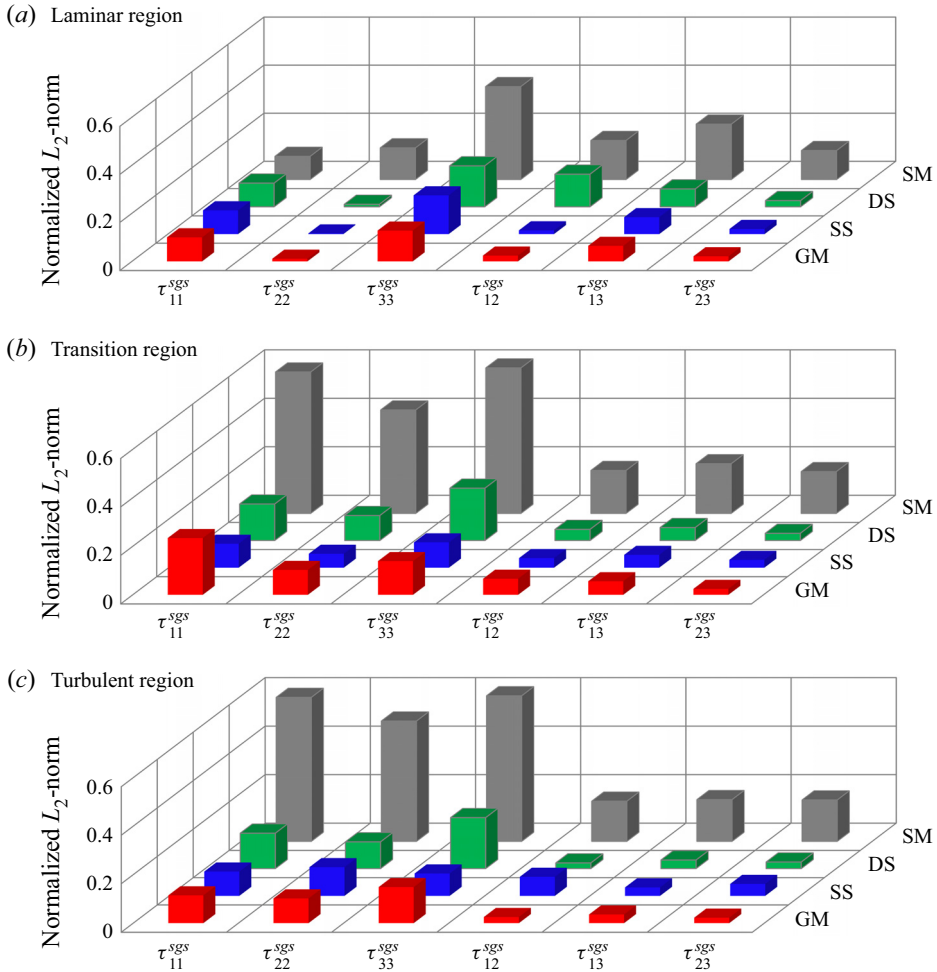


Figure 20. Normalized  $L_2$ -norm between the exact and the modelled  $\tau_{ij}^{SGS}$  at the (a) laminar region, (b) transition region and (c) turbulent region for  $M_c = 0.3$ .

following: first, isotropic turbulence is the necessary assumption for applying model SM; second, the Smagorinsky coefficient is constant over the entire domain; third, energy only transfers from resolved to SGS structures. We also present correlation coefficients for higher convective Mach number,  $M_c = 0.7$ , as seen in figure 19. In the laminar region, unlike the performance shown in the case with  $M_c = 0.3$ , all the models in general provide lower correlations. This trend can be explained with the characteristics of the flow field downstream of the trailing edge of the splitter plate. With the naturally developing boundary inlet condition, boundary layers evolve on the splitter plate, eventually encounter at the trailing edge and form a velocity deficit. The velocity deficit magnitude (VDM) and the velocity deficit presence distance (VDPD) increase as compressibility increases (Li *et al.* 2021). These phenomena affect the ability of the considered models to replicate the SGS stress components in the laminar region with high convective Mach numbers because the models are formulated based on the filtered velocity. In contrast, in the transition and turbulent regions, similar trends observed in figure 18 can also be found here. This observation implies that compressibility has an insignificant influence on the correlation

## Assessment of turbulence models using DNS data

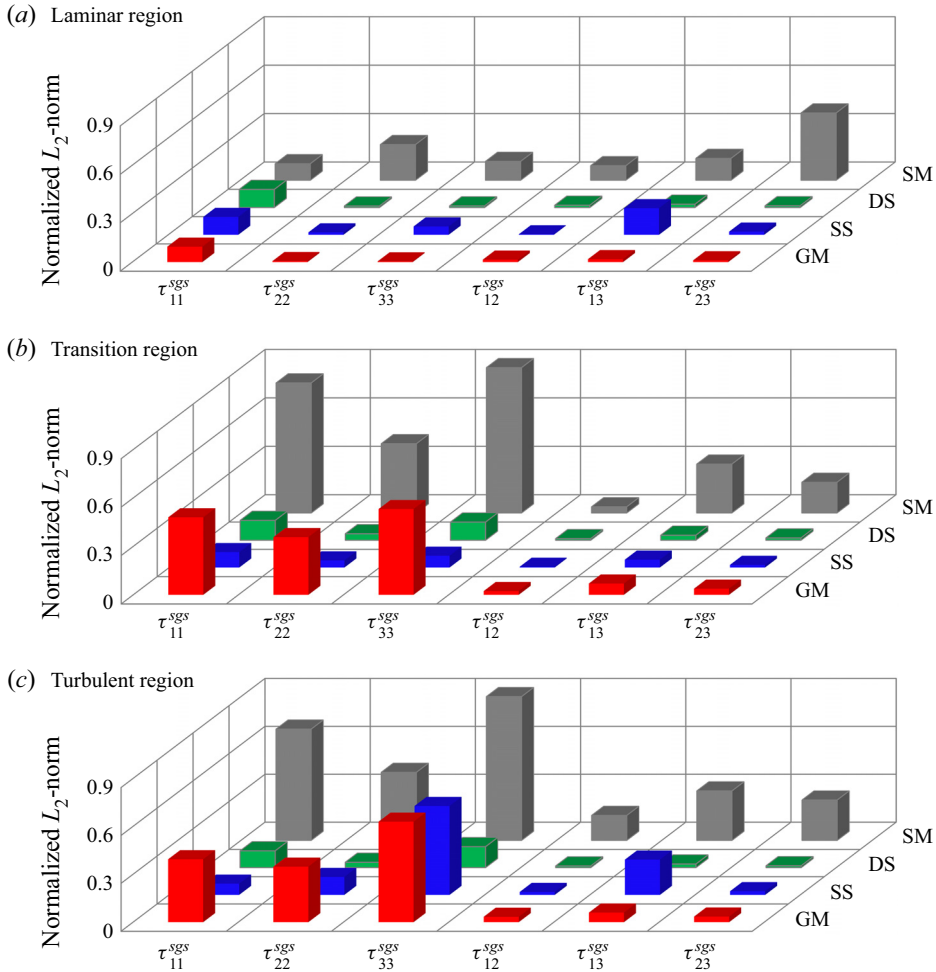


Figure 21. Normalized  $L_2$ -norm between the exact and the modelled  $\tau_{ij}^{sgs}$  at the (a) laminar region, (b) transition region and (c) turbulent region for  $M_c = 0.7$ .

coefficients of the SGS models in the transition and turbulent regions for the convective Mach numbers considered in this study.

In summary, for the cases with  $M_c = 0.3$  and  $0.7$ , SS and GM provide excellent correlations for the streamwise, cross-stream and spanwise normal SGS stress components in the entire flow domain. However, SS and GM show average correlations for all the shear SGS stress components. Model DS, which applies an eddy viscosity model with the scale similarity method, gives average correlations for nearly all SGS stress components in the transition and turbulent regions. Model SM, which merely uses the eddy viscosity model, provides low correlations for all SGS stress components in both the transition and turbulent region and gives average correlations in the laminar region for most of the SGS stress components. The correlation coefficient between the modelled and exact SGS stress indicates the quality of the reproduced spatial SGS structures. Therefore, models SS and GM can reproduce small-scale structures that satisfy the necessary interactions between small- and large-scale structures. In addition to presenting the correlation coefficients in terms of 3-D columns in figures 18 and 19, we also tabulate their magnitudes in

[Appendix A](#) for better quantitative comparisons between different models considered in this work.

### 5.2.2. $L_2$ -norm

Whether the model can accurately estimate the average quantity of the SGS stress is another important benchmark for an SGS model. In this context, we provide the normalized  $L_2$ -norm of the difference between the modelled and exact SGS stresses for  $M_c = 0.3$ , as shown in [figure 20](#). The compared models consist of SM, DS, SS and GM. The normalized  $L_2$ -norm results are separately calculated in the laminar, transition and turbulent regions, as indicated in [figures 20\(a\)](#), [20\(b\)](#) and [20\(c\)](#), respectively. For each stress component, we accumulate the discrepancies between two variables, namely the DNS and modelled SGS stresses, over the solution points in a flow region. The lower magnitude (significantly lower than unity) of the normalized  $L_2$ -norm indicates higher accuracy in prediction by the model. Models DS, SS and GM, in general, show higher accuracy than model SM for all stress components in all three regions because the model SM uses a constant eddy viscosity coefficient for the entire computational domain. Model DS also employs an eddy viscosity model, but shows high accuracy owing to its spatially and temporally self-adjusting eddy viscosity coefficient. Note that the magnitudes of the normalized  $L_2$ -norms are also tabulated in [Appendix B](#) for better quantitative comparisons between different models as well as various convective Mach numbers.

The results of the normalized  $L_2$ -norms for the case with  $M_c = 0.7$  are presented in [figure 21](#). As expected, the model SM, in general, gives poor performance for all of the SGS stresses and flow regions. Moreover, models SM and GM show smaller accumulated errors in the laminar region than those in the transition and turbulent regions. By further comparing [figure 21](#) with [figure 20](#) and the corresponding data in [Appendix B](#) ([tables 8](#) and [9](#)), we can see that models DS and SS show similar performance for  $M_c = 0.3$  and  $0.7$  in the transition and turbulent regions. This indicates that the accumulated errors from models DS and SS are insensitive to the change of the convective Mach number considered in this work. However, the accumulated errors from model SM for  $M_c = 0.7$  are, in general, larger than that from the case with  $M_c = 0.3$ , for nearly all SGS stresses in the entire flow field, based on the data in [tables 8](#) and [9](#) in [Appendix B](#). Interestingly, the accumulated discrepancy from the non-eddy viscosity model GM is slightly higher than that from models DS and SS for most of SGS stress components in the transition and turbulent regions for  $M_c = 0.7$ , which does not occur in the case with  $M_c = 0.3$ . Based on this observation, we suggest that an optimal coefficient should be added to the model GM ([5.29](#)) to account for the compressibility effects by applying the order-of-magnitude analysis (Fujiwara *et al.* 2000). However, this analysis needs to carry out the *a posteriori* test and therefore be considered as future work.

## 6. Summary and conclusions

The assessment of several typical turbulence models using DNS data has been carried out for  $M_c = 0.3$ ,  $0.5$  and  $0.7$ . The DNS data are generated by a high-order discontinuous spectral element method for a 3-D, spatially developing plane free shear layer. The shear layer is formed by two parallel streams separated by a splitter plate. The naturally developing inflow conditions on both sides of the splitter plate are the two fully developed Blasius boundary layers.

The considered turbulence models are evaluated through comparisons with the DNS data. For strong Reynolds analogy models, comparisons of the modelled cross-stream

profiles with DNS results show the following: excellent relation between temperature and velocity fluctuations; acceptable relations between the Favre and Reynolds velocity averages regardless of the convective Mach number. The temporal evolutions of the Favre and modelled velocity fluctuations show strong correlations at different locations across the shear layer in the turbulent region. Moreover, excellent agreement is obtained in the cross-stream profiles of the modelled and DNS shear stress for all considered Mach numbers. The extended strong Reynolds analogy models perform very well for the plane free shear layer.

The dilatational dissipation is insignificant in the plane free shear flow for the convective Mach numbers considered in this study. The examinations for the dilatational dissipation models indicate that none of the models can accurately predict the corresponding DNS results. Therefore, the considered models for dilatational dissipation are unsuitable for compressible plane free shear layer flows for  $M_c \leq 0.7$ . Several pressure–dilatation correlation models are also examined using the DNS data. The model by Huang *et al.* (1995) provides the best prediction, while the model by El Baz & Launder (1993) gives a large overestimate for both  $M_c = 0.3$  and  $0.7$ . In general, the considered models by Sarkar *et al.* (1992), El Baz & Launder (1993) and Huang *et al.* (1995) show more significant discrepancies with the DNS value as the convective Mach number increases from  $0.3$  to  $0.7$ .

The analysis of the Reynolds stress transport equations provides insights into the contributions of different stress components. In the streamwise normal stress transport equation, the pressure–strain correlation term is a significant sink term. In the cross-stream and spanwise normal stress transport equations, the turbulent production appears insignificant, while the pressure–strain correlation becomes the major source. The shear stress transport equation ( $i = 1$  and  $j = 2$ ) is dominated by the production and pressure–strain correlation terms. In the other shear stress equations, the production and pressure–strain correlation terms appear insignificant. The comparisons of the modelled and DNS cross-stream pressure–strain correlation profiles suggest that the considered models accurately estimate most of the pressure–strain correlation components. However, the compressibility modification model gives poor predictions for the high-Mach-number case.

The results of the *a priori* test for the SGS models are analysed quantitatively. The scale similarity and gradient models, which are the non-eddy viscosity models, can accurately reproduce different SGS stress components in terms of structure and magnitude. The dynamic model, which is the eddy viscosity model based on the scale similarity idea, shows acceptable correlation and accuracy for most SGS stress components for both  $M_c = 0.3$  and  $0.7$ . Finally, the Smagorinsky model, which is the purely dissipative model, gives low correlations and large accumulated errors.

**Acknowledgements.** The Advanced Cyberinfrastructure for Education and Research (ACER) at the University of Illinois at Chicago provided part of the computational resources for this study. This study was also supported by the Blue Waters sustained-petascale computing project sponsored by the National Science Foundation (awards OCI-0725070 and ACI-1238993) and the state of Illinois. Blue Waters is a joint effort of the University of Illinois at Urbana-Champaign and its National Center for Supercomputing Applications. The Program Development Company GridPro provided us with the license to access its meshing software, which was used to generate the meshes for the simulations presented in this work.

**Declaration of interests.** The authors report no conflict of interest.

**Author ORCIDs.**

 D. Li <https://orcid.org/0000-0001-5596-4374>;

 J. Komperda <https://orcid.org/0000-0002-8962-1828>;

Correlation coefficients for  $M_c = 0.3$




SGS stress	Laminar region				Transition region				Turbulent region			
	SM	DS	SS	GM	SM	DS	SS	GM	SM	DS	SS	GM
$\tau_{11}^{sgs}$	0.354	0.181	0.689	0.739	0.0652	0.477	0.899	0.754	0.128	0.408	0.681	0.917
$\tau_{22}^{sgs}$	0.516	0.575	0.673	0.677	0.226	0.547	0.893	0.939	0.001	0.501	0.738	0.950
$\tau_{33}^{sgs}$	0.980	0.912	0.833	0.743	0.238	0.574	0.853	0.912	0.111	0.513	0.883	0.914
$\tau_{12}^{sgs}$	0.003	0.289	0.324	0.523	0.061	0.118	0.278	0.164	0.097	0.302	0.494	0.232
$\tau_{13}^{sgs}$	0.049	0.025	0.323	0.407	0.037	0.089	0.248	0.283	0.091	0.058	0.252	0.315
$\tau_{23}^{sgs}$	0.711	0.410	0.002	0.365	0.004	0.103	0.485	0.546	0.068	0.205	0.458	0.459

Table 6. Correlation coefficient,  $R$ , for  $M_c = 0.3$  between the exact and the modelled SGS stresses by SM, DS, SS and GM, at the laminar region, transition region and turbulent region for  $M_c = 0.3$ .

Correlation coefficients for  $M_c = 0.7$

SGS stress	Laminar region				Transition region				Turbulent region			
	SM	DS	SS	GM	SM	DS	SS	GM	SM	DS	SS	GM
$\tau_{11}^{sgs}$	0.678	0.178	0.0677	0.392	0.104	0.582	0.755	0.832	0.138	0.607	0.779	0.892
$\tau_{22}^{sgs}$	0.279	0.535	0.005	0.372	0.050	0.632	0.837	0.950	0.043	0.551	0.819	0.923
$\tau_{33}^{sgs}$	0.812	0.186	0.003	0.980	0.390	0.642	0.740	0.905	0.0946	0.682	0.761	0.879
$\tau_{12}^{sgs}$	0.009	0.124	0.003	0.428	0.009	0.782	0.360	0.446	0.126	0.533	0.358	0.270
$\tau_{13}^{sgs}$	0.252	0.407	0.002	0.733	0.039	0.005	0.141	0.432	0.021	0.005	0.167	0.235
$\tau_{23}^{sgs}$	0.391	0.151	0.001	0.053	0.144	0.339	0.244	0.246	0.196	0.380	0.219	0.248

Table 7. Correlation coefficient,  $R$ , for  $M_c = 0.7$  between the exact and the modelled SGS stresses by SM, DS, SS and GM, at the laminar region, transition region and turbulent region for  $M_c = 0.7$ .

-  A. Peyvan <https://orcid.org/0000-0003-4038-3432>;
-  Z. Ghiasi <https://orcid.org/0000-0002-4186-0475>;
-  F. Mashayek <https://orcid.org/0000-0003-1187-4937>.

### Appendix A. Correlation coefficients

The analysis of the correlation coefficient  $R$  is one of our approaches to assess the performance of the considered SGS models in this work. The correlation coefficient between the modelled and exact stress reveals the ability of the model to capture the turbulent spatial structure. The magnitude of  $R$  ranges from 0 to 1. Magnitudes near unity represent a high correlation. A decrease in the magnitude of  $R$  value indicates a loss of ability to capture the flow structure. We separately investigate the performance of the SGS models in the laminar region, transition region and turbulent region owing to the large difference in the behaviours of laminar and turbulent flows. In addition to presenting the correlation coefficients in terms of 3-D columns in figures 18 and 19, we also tabulate their magnitudes in tables 6 and 7 for better quantitative comparisons between different models considered in this work.



Normalized  $L_2$ -norms for  $M_c = 0.3$

SGS stress	Laminar region				Transition region				Turbulent region			
	SM	DS	SS	GM	SM	DS	SS	GM	SM	DS	SS	GM
$\tau_{11}^{sgs}$	0.096	0.097	0.099	0.100	0.583	0.151	0.099	0.234	0.593	0.146	0.100	0.115
$\tau_{22}^{sgs}$	0.132	0.010	0.003	0.011	0.427	0.103	0.057	0.103	0.496	0.110	0.118	0.102
$\tau_{33}^{sgs}$	0.386	0.170	0.161	0.128	0.816	0.216	0.104	0.139	0.820	0.210	0.092	0.149
$\tau_{12}^{sgs}$	0.162	0.136	0.016	0.024	0.177	0.046	0.040	0.066	0.165	0.023	0.079	0.025
$\tau_{13}^{sgs}$	0.230	0.074	0.070	0.065	0.205	0.054	0.053	0.056	0.172	0.035	0.035	0.036
$\tau_{23}^{sgs}$	0.120	0.026	0.021	0.021	0.172	0.030	0.032	0.024	0.170	0.027	0.049	0.023

Table 8. Normalized  $L_2$ -norm for  $M_c = 0.3$  between the exact and the modelled  $\tau_{ij}^{sgs}$  at the (a) laminar region, (b) transition region and (c) turbulent region.

Normalized  $L_2$ -norms for  $M_c = 0.7$

SGS stress	Laminar region				Transition region				Turbulent region			
	SM	DS	SS	GM	SM	DS	SS	GM	SM	DS	SS	GM
$\tau_{11}^{sgs}$	0.102	0.112	0.111	0.096	0.805	0.123	0.095	0.480	0.696	0.105	0.070	0.394
$\tau_{22}^{sgs}$	0.221	0.009	0.015	0.006	0.429	0.040	0.044	0.358	0.426	0.033	0.112	0.348
$\tau_{33}^{sgs}$	0.117	0.010	0.052	0.005	0.930	0.112	0.073	0.531	0.918	0.131	0.557	0.629
$\tau_{12}^{sgs}$	0.090	0.014	0.003	0.015	0.038	0.010	0.005	0.023	0.156	0.010	0.018	0.034
$\tau_{13}^{sgs}$	0.135	0.020	0.165	0.018	0.302	0.031	0.049	0.070	0.310	0.023	0.221	0.060
$\tau_{23}^{sgs}$	0.416	0.011	0.020	0.011	0.190	0.014	0.016	0.038	0.252	0.012	0.023	0.035

Table 9. Normalized  $L_2$ -norm for  $M_c = 0.7$  between the exact and the modelled  $\tau_{ij}^{sgs}$  at the (a) laminar region, (b) transition region and (c) turbulent region.

## Appendix B. $L_2$ -norms

We also evaluate the performance of the considered SGS models via the analysis of the normalized discrete  $L_2$ -norm. The normalized  $L_2$ -norm of the difference between the modelled SGS stress and the exact SGS stress by filtering the DNS data indicates whether the model is able to correctly predict the average value of the SGS stress. A larger normalized  $L_2$ -norm indicates a loss of ability to accurately capture the magnitude of the SGS stress. The performance of the SGS models in the laminar region, transition region and turbulent region is separately investigated owing to the fact that the flow behaviours are distinctly different in those regions. In addition to presenting the normalized  $L_2$ -norm as 3-D columns in figures 20 and 21, their values are also tabulated in tables 8 and 9 for better quantitative comparisons between different models and convective Mach numbers.

## REFERENCES

- BARDINA, J., FERZIGER, J.H. & REYNOLDS, W.C. 1980 Improved subgrid scale models for large eddy simulation. *AIAA Paper* 80-1357.
- BARRE, S. & BONNET, J.P. 2015 Detailed experimental study of a highly compressible supersonic turbulent plane mixing layer and comparison with most recent DNS results: "towards an accurate description of compressibility effects in supersonic free shear flows". *Intl J. Heat Fluid Flow* **51**, 324–334.

- BARRE, S., QUINE, C. & DUSSAUGE, J.P. 1994 Compressibility effects on the structure of supersonic mixing layers: experimental results. *J. Fluid Mech.* **259**, 47–78.
- BOGDANOFF, D.W. 1983 Compressibility effects in turbulent shear layers. *AIAA J.* **21**, 926–927.
- BOUFFANAIS, R., DEVILLE, M.O., FISCHER, P.F., LERICHE, E. & WEILL, D. 2006 Large-eddy simulation of the lid-driven cubic cavity flow by the spectral element method. *J. Sci. Comput.* **27**, 151–162.
- BRADSHAW, P. 1966 The effect of initial conditions on the development of a free shear layer. *J. Fluid Mech.* **26**, 225–236.
- BRADSHAW, P. 1977 Compressible turbulent shear layers. *Annu. Rev. Fluid Mech.* **9**, 33–54.
- BROWN, C.S., SHAVER, D.R., LAHEY, R.T. & BOLOTNOV, I.A. 2017 Wall-resolved spectral cascade-transport turbulence model. *Nucl. Sci. Engng* **320**, 309–324.
- BURTON, G.C. & DAHM, W.J.A. 2005 Multifractal subgrid-scale modeling for large-eddy simulation. I. Model development and a priori testing. *Phys. Fluids* **17**, 075111.
- CARLSON, J. 2005 Assessment of an explicit algebraic Reynolds stress model. NASA, Langley Research Center, Hampton, Virginia TM-2005-213771.
- CARPENTER, M.H. & KENNEDY, C.A. 1994 Fourth-order 2N-storage Runge–Kutta schemes. NASA TM 109112.
- CEBECI, T. & SMITH, A.M.O. 1974 *Analysis of Turbulent Boundary Layers*. Academic Press, Inc.
- CECORA, R.D., EISFELD, B., PROBST, A., CRIPPA, S. & RADESPIEL, R. 2012 Differential Reynolds stress modeling for aeronautics. *AIAA Paper* 2012-0465.
- CLARK, R.A., FERZIGER, J.H. & REYNOLDS, W.C. 1979 Evaluation of subgrid-scale models using an accurately simulated turbulent flow. *J. Fluid Mech.* **91**, 1–16.
- DALY, B.J. & HARLOW, F.H. 1970 Transport equations of turbulence. *Phys. Fluids* **13**, 2634–2649.
- DEARDROFF, J.W. 1970 A numerical study of three-dimensional turbulence channel flow at large Reynolds number. *J. Fluid Mech.* **41**, 452–456.
- DUAN, L. & MARTIN, M.P. 2011 Direct numerical simulation of hypersonic turbulent boundary layers. Part 4. Effect of high enthalpy. *J. Fluid Mech.* **684**, 25–59.
- DUDEK, J.C. & CARLSON, J. 2017 Evaluation of full Reynolds stress turbulence models in FUN3D. NASA, Langley Research Center, Hampton, Virginia TM-2017-219468.
- EL BAZ, A.M.E.L. & LAUNDER, B.E. 1993 Second-moment modelling of compressible mixing layers. In *Engineering Turbulence Modelling and Experiments*, pp. 63–72. Elsevier.
- FAVRE, A. 1965 The equations of compressible turbulent gases. Annual Summary Report AD0622097.
- FAVRE, A. 1969 Statistical equations of turbulent gases. In *Problems of Hydrodynamics and Continuum Mechanics*, pp. 231–266. SIAM.
- FAVRE, A. 1983 Turbulence: space-time statistical properties and behavior in supersonic flows. *Phys. Fluids* **26**, 2851–2863.
- FUJIWARA, H., MATSUO, Y. & ARAKAWA, C. 2000 A turbulence model for the pressure-strain correlation term accounting for compressibility effects. *Intl J. Heat Fluid Flow* **21**, 354–358.
- GAVIGLIO, J. 1987 Reynolds analogies and experimental study of heat transfer in the supersonic boundary layer. *Intl J. Heat Mass Transfer* **30**, 911–926.
- GERMANO, M., PIOMELLI, U., MOIN, P. & CABOT, W.H. 1991 A dynamic subgrid scale eddy viscosity model. *Phys. Fluids A* **3** (7), 1760–1765.
- GHIASI, Z., KOMPERDA, J., LI, D., PEYVAN, A., NICHOLLS, D. & MASHAYEK, F. 2019 Modal explicit filtering for large eddy simulation in discontinuous spectral element method. *J. Comput. Phys.: X* **3**, 100024.
- GHOSAL, S., LUND, T., MOIN, P. & AKSELVOL, K. 1995 A dynamic localisation model for large-eddy simulation of turbulent flows. *J. Fluid Mech.* **286**, 229–255.
- GHOSAL, S. & MOIN, P. 1995 The basic equations for the large eddy simulation of turbulent flows in complex geometry. *J. Comput. Phys.* **118**, 24–37.
- GIRIMAJI, S.S. 2000 Pressure-strain correlation modelling of complex turbulent flows. *J. Fluid Mech.* **422**, 91–123.
- GOEBEL, S.G. & DUTTON, J.C. 1991 Experimental study of compressible turbulent mixing layers. *AIAA J.* **29**, 538–546.
- GROSS, N., BLAISDELL, G.A. & LYRINTZIS, A.S. 2011 Analysis of modified compressibility corrections for turbulence models. *AIAA Paper* 2011-279.
- GRUBER, M.R., MESSERSMITH, N.L. & DUTTON, J.C. 1993 Three-dimensional velocity field in a compressible mixing layer. *AIAA J.* **31**, 2061–2067.
- GULLBRAND, J. & CHOW, F.K. 2003 The effect of numerical errors and turbulence models in large-eddy simulations of channel flow, with and without explicit filtering. *J. Fluid Mech.* **495**, 323–341.
- HAASE, W., AUPOIX, B., BUNGE, U. & SCHWAMBORN, D. 2006 FLOMANIA – a European initiative on flow physics modelling. In *Notes on Numerical Fluid Mechanics and Multidisciplinary Design*, vol. 218. Springer.

## Assessment of turbulence models using DNS data

- HANJALIC, K. & LAUNDER, B.E. 1976 Contribution towards a Reynolds-stress closure for low-Reynolds-number turbulence. *J. Fluid Mech.* **74**, 593–610.
- HUANG, P.G., COLEMAN, G.N. & BRADSHAW, P. 1995 Compressible turbulent channel flows: DNS results and modelling. *J. Fluid Mech.* **305**, 185–218.
- HWANG, R.R. & JAW, S.Y. 1998 Second-order closure turbulence models: their achievements and limitations. *Proc. Natl Sci. Counc. ROC(A)* **22**, 703–722.
- JACOBS, G.B. 2003 Numerical simulation of two-phase turbulent compressible flows with a multidomain spectral method. Ph.D. Thesis, University of Illinois at Chicago, Chicago, IL.
- JACOBS, G.B., KOPRIVA, D.A. & MASHAYEK, F. 2003 A comparison of outflow boundary conditions for the multidomain staggered-grid spectral method. *Numer. Heat Transfer B* **44** (3), 225–251.
- JACOBS, G.B., KOPRIVA, D.A. & MASHAYEK, F. 2005 Validation study of a multidomain spectral code for simulation of turbulent flows. *AIAA J.* **43**, 1256–1264.
- JAW, S.Y. & CHEN, C.J. 1998*a* Present status of second-order closure turbulence models. I: overview. *J. Engng Mech.* **124**, 485–501.
- JAW, S.Y. & CHEN, C.J. 1998*b* Present status of second order closure turbulence models. II: applications. *J. Engng Mech.* **124**, 502–512.
- JIMÉNEZ, J. 2004 Turbulence and vortex dynamics. *Notes for the Polytechnic Course on Turbulence*. École Polytechnique, Paris.
- KOMPERDA, J., GHIASI, Z., LI, D., PEYVAN, A., JABERI, F. & MASHAYEK, F. 2020 A hybrid discontinuous spectral element method and filtered mass density function solver for turbulent reacting flows. *Numer. Heat Transfer B-Fund.* **78**, 1–29.
- KOPRIVA, D.A. 1998 A staggered-grid multidomain spectral method for the compressible Navier–Stokes equations. *J. Comput. Phys.* **143**, 125–158.
- KOPRIVA, D.A. & KOLIAS, J.H. 1996 A conservative staggered-grid Chebyshev multidomain method for compressible flows. *J. Comput. Phys.* **125**, 244–261.
- LAUNDER, B.E. 1989 Second-moment closure: present . . . and future? *Intl J. Heat Fluid Flow* **10**, 282–300.
- LAUNDER, B.E., REECE, G.J. & RODI, W. 1975 Progress in the development of Reynolds stress turbulence closure. *J. Fluid Mech.* **68**, 537–566.
- LELE, S.K. 1994 Compressibility effects on turbulence. *Annu. Rev. Fluid Mech.* **26**, 211–254.
- LEONARD, A. 1975 Energy cascade in large eddy simulation of turbulent fluid flow. *Adv. Geophys.* **18**, 237–248.
- LEONARD, A. 1997 Large eddy simulation of chaotic convection and beyond. *AIAA Paper* 97-0204.
- LI, D., KOMPERDA, J., GHIASI, Z., PEYVAN, A. & MASHAYEK, F. 2019 Compressibility effects on the transition to turbulence in spatially developing plane free shear layer. *Theor. Comput. Fluid Dyn.* **33**, 577–602.
- LI, D., PEYVAN, A., GHIASI, Z., KOMPERDA, J. & MASHAYEK, F. 2021 Compressibility effects on energy exchange mechanisms in a spatially developing plane free shear layer. *J. Fluid Mech.* **910**, A9.
- LILLY, D.K. 1966 On the application of the eddy viscosity concept in the inertial sub-range of turbulence. NCAR Manuscript 123.
- LILLY, D.K. 1992 A proposed modification of the Germano subgrid-scale closure method. *Phys. Fluids A* **4**, 633–635.
- LIU, S., MENEVEAU, C. & KATZ, J. 1994 On the properties of similarity subgrid-scale models as deduced from measurements in a turbulent jet. *J. Fluid Mech.* **275**, 83–119.
- LOVE, M.D. 1980 Subgrid modelling studies with Burgers' equation. *J. Fluid Mech.* **100**, 87–100.
- LU, H., RUTLAND, C.J. & SMITH, L.M. 2007 Correlation and causation. *J. Turbul.* **8**, 1–27.
- MOIN, P., SQUIRES, K., CABOT, W. & LEE, S. 1991 A dynamic subgrid model for compressible turbulence and scalar transport. *Phys. Fluids A* **3**, 2746–2757.
- MORKOVIN, M.V. 1962 Effects of compressibility on turbulent flows. In *Mécanique de la Turbulence* (ed. A.J. Favre), pp. 367–380. CNRS.
- NICOD, F. & DUCROS, F. 1999 Subgrid-scale stress modelling based on the square of the velocity gradient. *Flow Turbul. Combust.* **62**, 183–200.
- NICOD, F., TODA, H.B., CABRIT, O., BOSE, S. & LEE, J. 2011 Using singular values to build a subgrid-scale model for large eddy simulation. *Phys. Fluids* **23**, 085106.
- OKONG'O, N. & BELLAN, J. 2004 Consistent large-eddy simulation of a temporal mixing layer laden with evaporating drops. Part 1. Direct numerical simulation, formulation and a priori analysis. *J. Fluid Mech.* **499**, 1–47.
- PANTANO, C. & SARKAR, S. 2002 A study of compressibility effects in the high-speed turbulent shear layer using direct simulation. *J. Fluid Mech.* **451**, 329–371.

- PIOMELLI, U., CABOT, W.H., MOIN, P. & LEE, S. 1990 Subgrid-scale backscatter in transitional and turbulent flows. In *Proceedings of the 1990 Summer Program*, pp. 19–30. Center for Turbulence Research.
- PIOMELLI, U., CABOT, W.H., MOIN, P. & LEE, S. 1991 Subgrid-scale backscatter in turbulent and transitional flows. *Phys. Fluids A* **3** (7), 1766–1771.
- PIOMELLI, U. & ZANG, T.A. 1991 Large-eddy simulation of transitional channel flow. *Comput. Phys. Commun.* **65**, 224–230.
- POPE, S.B. 2000 *Turbulent Flows*. Cambridge University Press.
- REYNOLDS, O. 1895 On the dynamical theory of incompressible viscous fluids and the determination of the criterion. *Philos. Trans. R. Soc. Lond. A* **186**, 123–164.
- RISTORCELLI, J.R., LUMLEY, J.L. & ABID, R. 1995 A rapid-pressure covariance representation consistent with the Taylor–Proudman theorem materially frame indifferent in two-dimensional limit. *J. Fluid Mech.* **298**, 211–248.
- SARKAR, S., ERLEBACHER, G. & HUSSAINI, M.Y. 1992 Compressible homogeneous shear: simulation and modeling. NASA, Langley Research Center, Hampton, Virginia NAS1-18605.
- SARKAR, S., ERLEBACHER, G., HUSSAINI, M.Y. & KREISS, H.O. 1989 The analysis and modeling of dilatational terms in compressible turbulence. NASA, Langley Research Center, Hampton, Virginia NAS1-18605.
- SARKAR, S., ERLEBACHER, G., HUSSAINI, M.Y. & KREISS, H.O. 1991 The analysis and modelling of dilatational terms in compressible turbulence. *J. Fluid Mech.* **227**, 473–493.
- SCHEFFEL, J. 2001 On analytical solution of the Navier–Stokes equations. Royal Institute of Technology, Stockholm, Sweden TRITA-ALE-2001-01.
- SCHMIDT, H. & SCHUMANN, U. 1989 Coherent structure of the convective boundary layer derived from large-eddy simulations. *J. Fluid Mech.* **200**, 511–562.
- SELLE, L., OKONG’O, N., BELLAN, J. & HARSTAD, K. 2007 Modelling of subgrid-scale phenomena in supercritical transitional mixing layers: an a priori study. *J. Fluid Mech.* **593**, 57–91.
- SMAGORINSKY, J. 1963 General circulation experiments with the primitive equations: I. The basic equations. *Mon. Weath. Rev.* **91**, 99.
- SMITS, A.J. & DUSSAUGE, J.P. 2006 *Turbulent Shear Layers in Supersonic Flow*. Springer Science.
- SMYTH, W.D. & MOUM, J.N. 2000 Anisotropy of turbulence in stably stratified mixing layers. *Phys. Fluids* **12**, 1343–1362.
- SPEZIALE, C.G. 1985 Galiean invariance of subgrid-scale stress models in the large-eddy simulation of turbulence. *J. Fluid Mech.* **156**, 55–62.
- SPEZIALE, C.G., SARKAR, S. & GATSKI, T.B. 1991 Modelling the pressure-strain correlation of turbulence: an invariant dynamical systems approach. *J. Fluid Mech.* **227**, 245–272.
- THOMPSON, K.W. 1987 Time dependent boundary conditions for hyperbolic systems. *J. Comput. Phys.* **68**, 1–24.
- VREMAN, B., GEURTS, B. & KUERTEN, H. 1995a A priori tests of large eddy simulation of the compressible plane mixing layer. *J. Engng Maths* **29**, 299–327.
- VREMAN, B., GEURTS, B.J. & KUERTEN, H. 1995b Subgrid-modeling in LES of compressible flow. *Appl. Sci. Res.* **54**, 191–203.
- VREMAN, B., GEURTS, B. & KUERTEN, H. 1997 Large-eddy simulation of the turbulent mixing layer. *J. Fluid Mech.* **339**, 357–390.
- VREMAN, A.W., SANDHAM, N.D. & LUO, K.H. 1996 Compressible mixing layer growth rate and turbulence characteristics. *J. Fluid Mech.* **320**, 235–258.
- WILCOX, D.C. 1992 Dilatation-dissipation corrections for advanced turbulence models. *AIAA J.* **30**, 2639–2646.
- WILCOX, D.C. 2006 *Turbulence Modeling for CFD*, 3rd edn. DCW Industries.
- WRIGHT, S. 1921 Correlation and causation. *J. Agric. Res.* **20**, 557–585.
- XU, X. 2003 Large eddy simulation of compressible turbulent pipe flow with heat transfer. PhD Thesis, Iowa State University, Iowa.
- YODER, D.A. 2003 Initial evaluation of an algebraic Reynolds stress model for compressible turbulent shear flows. *AIAA Paper* 2003-548.
- ZANG, T.A., DAHLBURG, R.B. & DAHLBURG, J.P. 1992 Direct and large-eddy simulations of three-dimensional compressible Navier–Stokes turbulence. *Phys. Fluids A* **4**, 127–140.
- ZEMAN, O. 1990 Dilatation dissipation: the concept and application in modeling compressible mixing layers. *Phys. Fluids A* **2**, 178–188.
- ZHANG, Y.S., BI, W.T., HUSSAIN, F. & SHE, Z.S. 2014 A generalized Reynolds analogy for compressible wall-bounded turbulent flows. *J. Fluid Mech.* **739**, 392–420.